Article

GaAs nano-ridge laser diodes fully fabricated in a 300-mm CMOS pilot line

Yannick De Koninck[1,4,10], Charles Caer[1,5,10 ✉], Didit Yudistira[1,10 ✉], Marina Baryshnikova[1], Huseyin Sar[1], Ping-Yi Hsieh[1,2], Cenk Ibrahim Özdemir[1,3,6], Saroj Kanta Patra[1,7], Nadezda Kuznetsova[1,8], Davide Colucci[1,3], Alexey Milenin[1], Andualem Ali Yimam[3], Geert Morthier[3], Dries Van Thourhout[3], Peter Verheyen[1], Marianna Pantouvaki[1,9], Bernardette Kunert[1 ✉] & Joris Van Campenhout[1 ✉]

Silicon photonics is a rapidly developing technology that promises to revolutionize the way we communicate, compute and sense the world[1–6]. However, the lack of highly scalable, native complementary metal–oxide–semiconductor (CMOS)-integrated light sources is one of the main factors hampering its widespread adoption. Despite considerable progress in hybrid and heterogeneous integration of III–V light sources on silicon[7–12], monolithic integration by direct epitaxy of III–V materials remains the pinnacle of cost-effective on-chip light sources. Here we report the electrically driven gallium arsenide (GaAs)-based laser diodes fully fabricated on 300-mm Si wafers in a CMOS pilot manufacturing line based on a new integration approach, nano-ridge engineering. GaAs nano-ridge waveguides with embedded p–i–n diodes and InGaAs quantum wells are grown at high quality on a wafer scale. Room-temperature continuous-wave lasing is demonstrated at wavelengths around 1,020 nm in more than 300 devices across a wafer, with threshold currents as low as 5 mA, output powers beyond 1 mW, laser linewidths down to 46 MHz and laser operation up to 55 °C. These results illustrate the potential of the III–V/Si nano-ridge engineering concept for the monolithic integration of laser diodes in a Si photonics platform, enabling future cost-sensitive high-volume applications in optical sensing, interconnects and beyond.

Silicon photonics enables the miniaturization and mass manufacturing of optical systems for a growing set of applications[13–16]. However, the lack of native, low-cost coherent light sources is a major roadblock for ubiquitous adoption of the technology, especially for future high-volume cost-sensitive applications, such as chip-to-chip optical interconnects in machine-learning systems[17], fibre-to-the-X applications[18] or optical sensors for consumer devices[19]. In many of today's datacom products, lasers are manufactured and tested separately on their native III–V substrates, and subsequently hybrid integrated on the silicon photonics wafers in micro-assembled laser packages[20] or through high-precision flip-chip assembly[7–9]. Owing to the sequential nature and high-precision requirement of such assembly processes, the manufacturing throughput of these integration solutions may not scale to meet the aggressive density, cost and volume targets for future products. To address these challenges, various hybrid and heterogeneous III–V integration techniques are being developed and commercialized at present, such as micro-transfer printing[21] or heterogeneous III–V integration, involving die-to-wafer bonding of non-patterned III–V layer stacks directly on the silicon photonics wafer that has been thoroughly developed over the past several years[10–12] and is now available in at least two commercial manufacturing lines[22,23]. However, deep cost reductions and wide adoption of this technology

in mainstream complementary metal-oxide semiconductor (CMOS) foundries may be hampered by the remaining need for die-to-wafer bonding and expensive III–V donor substrates used for epitaxial III–V growth, generating waste during the manufacturing process, raising further concerns around health, safety and environmental sustainability.

For these reasons, direct epitaxy of high-quality III–V materials selectively at the desired locations on large-size silicon photonics wafers remains a highly sought-after objective. Unfortunately, the large mismatch in crystal lattice parameters and thermal expansion coefficients between III–V and Si materials inevitably initiates the formation of crystal misfit defects, known to deteriorate laser performance and reliability. To reduce the defectivity in the III–V layers, many research groups have developed thick buffer layers and strained superlattice layers with great success[24–26]. Gallium arsenide (GaAs)-based stacks featuring indium arsenide (InAs) quantum-dot gain regions have unlocked tremendous progress in the performance and reliability of monolithically integrated lasers on Si, leveraging the improved tolerance of quantum-dots against residual crystal defects[27,28]. However, these results have been limited to die-level demonstrations only. Thick buffer layers are difficult to implement on large-diameter wafers because of layer cracking and other defects arising from thermally induced stress.

[1]imec, Leuven, Belgium. [2]KU Leuven, Leuven, Belgium. [3]Photonics Research Group, Ghent University–imec, Ghent, Belgium. [4]Present address: NVidia Corporation, Roskilde, Denmark. [5]Present address: Centre Suisse d'Electronique et de Microtechnique SA (CSEM), Neuchâtel, Switzerland. [6]Present address: Infinera Corporation, Sunnyvale, CA, USA. [7]Present address: AMS-OSRAM International GmbH, Regensburg, Germany. [8]Present address: SMART Photonics, Eindhoven, The Netherlands. [9]Present address: Microsoft Corporation, Cambridge, UK. [10]These authors contributed equally: Yannick De Koninck, Charles Caer, Didit Yudistira. ✉e-mail: charles.caer@csem.ch; didit.yudistira@imec.be; bernardette.kunert@imec.be; joris.vancampenhout@imec.be
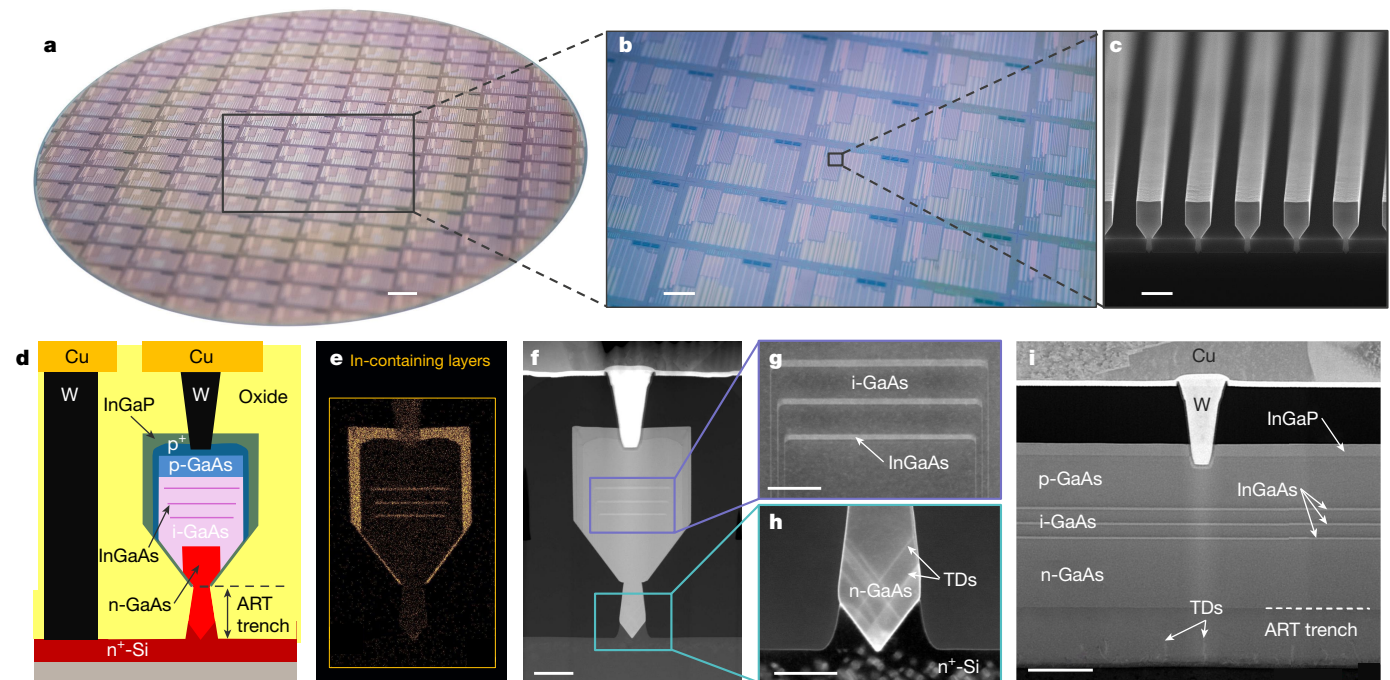
Fig. 1 | Wafer-scale integration of GaAs NR lasers on Si. a, Photograph of a fabricated 300-mm Si wafer containing thousands of GaAs devices. **b**, Close-up view of a fabricated 300-mm wafer showing several dies. **c**, Cross-sectional scanning electron micrograph of a GaAs NR array after epitaxy and before encapsulation in oxide. **d**, Sketch of the cross-section of a GaAs NR device highlighting the various layers, including the InGaAs quantum wells, p–i–n diode, InGaP passivation layer and metal contacts. **e**, Energy-dispersive X-ray spectroscopy image of a NR cross-section highlighting the In-containing layers near the Lα X-ray peaks. **f**, HAADF-STEM image of a transverse cut of a GaAs NR device. **g**, DF-STEM close-up view of the InGaAs quantum wells embedded in the non-intentionally-doped GaAs. **h**, DF-STEM close-up view of the n-GaAs–n-Si interface confirming ART of threading dislocation (TD) defects. **i**, HAADF-STEM image of a longitudinal cut of a NR device, showing an isolated W plug contacting the p-GaAs layer. Scale bars: 2.5 cm (**a**); 1 cm (**b**); 1 μm (**c**); 200 nm (**f**,**i**); 100 nm (**g**,**h**).

Recently, encouraging extensions of this work have been reported, featuring epitaxy in deep pockets etched in a silicon-oxide masking layer on 300- (ref. 29) and 200-mm silicon photonics wafers[30]. However, the molecular-beam epitaxy process for growing the quantum-dot stack is intrinsically non-selective, resulting in the deposition of a polycrystalline III–V film outside the targeted trenches, potentially hampering subsequent wafer-scale integration processes.

Selective-area growth of III–V materials on patterned Si wafers by metal-organic vapour-phase epitaxy (MOVPE) represents a compelling integration approach, arguably with better scalability potential than molecular-beam epitaxy. Selectivity can be easily achieved in vapour-phase epitaxy and, as such, the III–V material can be deposited only where needed. The confinement of misfit defects is achieved by starting the growth of the III–V layers in deep and narrow trenches etched in a dielectric masking layer on the Si wafer, a technique referred to as aspect-ratio trapping (ART)[31–33]. Various ART architectures are being explored at present and efficient defect reduction has been reported without the need for thick buffer layers[34–36], consequently alleviating issues with wafer warpage and crack formation in the wafer-scale deposited III–V layers. Over recent years, we have developed the concept of nano-ridge (NR) engineering (NRE), a selective-area growth-based integration approach applying ART for defect reduction, followed by the growth of low-defectivity III–V NRs outside the trenches. By careful tuning of the MOVPE process parameters, the NR dimensions, shapes and composition can be accurately engineered. Optimized NR structures typically feature threading dislocation density (TDD) well below 10^5 cm^{-2}, up to 100 times lower than for optimized blanket buffer layers (Methods). Previously, we successfully applied NRE to realize a variety of heterostructures, in situ doping profiles and surface passivation layers in III–V material systems such as GaAs, InAs, GaSb and InGaAs[37–43], leading to some of the first device demonstrations including optically pumped lasers[44], heterojunction bipolar transistors[45] and wafer-scale GaAs-on-Si photodetectors with record-low dark currents[46].

Here we leverage the NRE concept to demonstrate full wafer-scale growth and fabrication of electrically pumped GaAs-based lasers on standard 300-mm Si (001) wafers, entirely on a CMOS pilot manufacturing line. Leveraging the low defectivity in GaAs NR structures, the NR lasers (NRLs) use an optical gain region based on In$_{0.2}$Ga$_{0.8}$As multiple quantum wells, embedded in an in situ doped p–i–n diode and effectively passivated with an InGaP capping layer, all monolithically grown on 300-mm Si wafers. Using on-wafer GaAs NR photodetectors (NRPDs) for wafer-level measurements, more than 300 NRLs showed continuous-wave lasing around 1,020 nm at room temperature, with threshold currents as low as 5 mA, slope efficiencies as high as 0.5 W A^{-1} and up to 1.76 mW total emitted optical power. Furthermore, an early reliability test revealed continuous-wave lasing during at least 500 h of room-temperature operation, with only a mild increase in threshold current and constant slope efficiency. We believe that these proof-of-concept results based on a new integration concept represent a major milestone towards the manufacturing of interconnects, optical sensors and beyond.

Laser structure and fabrication

Leveraging wafer-scale processes, several thousands of GaAs NR devices including lasers, photodetectors and test structures are fabricated on a standard 300-mm silicon wafer, as shown in Fig. 1a–c. Each GaAs NR structure is formed by NRE, initiated with the growth of n-type doped GaAs in a high aspect-ratio trench patterned in the n-doped silicon substrate (Fig. 1c). NRE allows to form fully relaxed box-shaped NR structures with embedded p–i–n heterojunction outside the trench. The gain
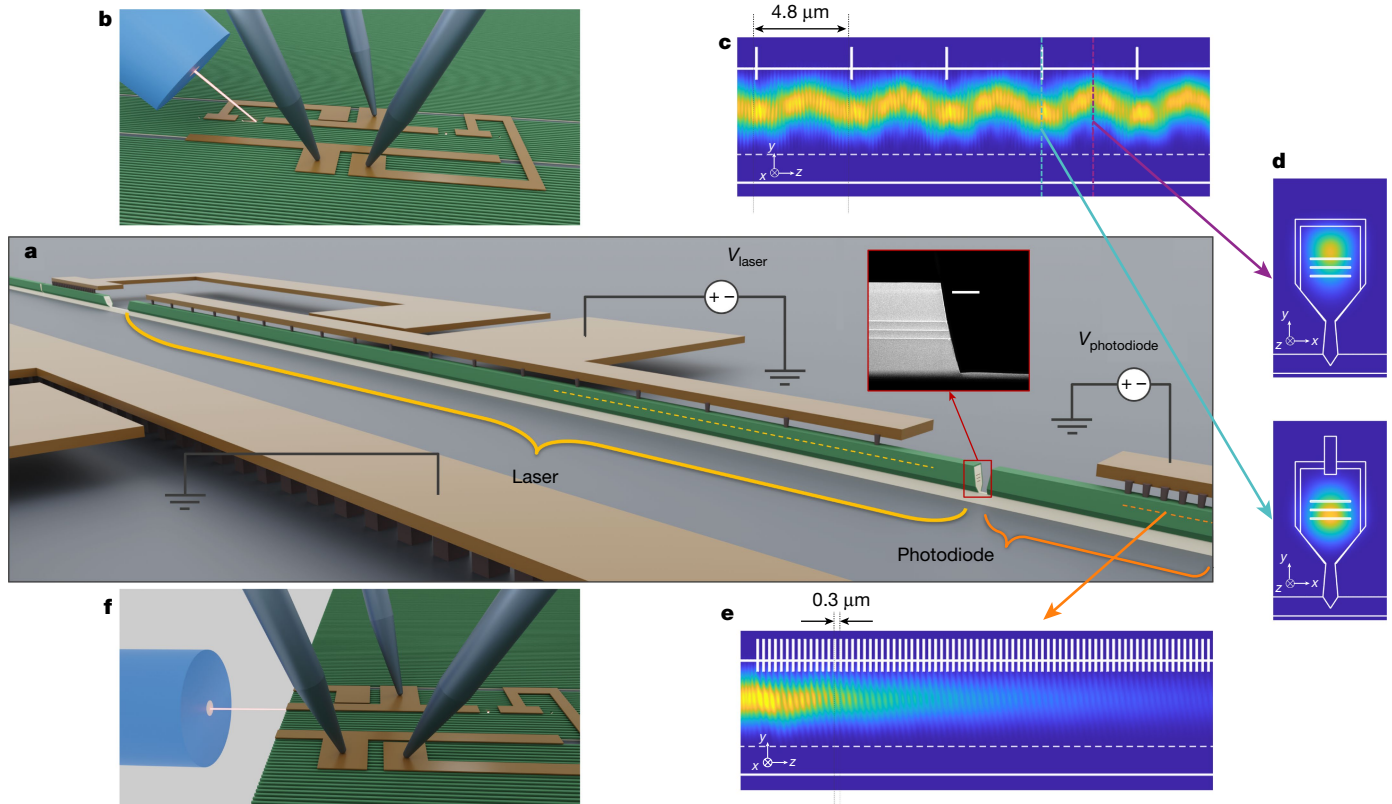
Fig. 2 | GaAs NR laser test cell with on-wafer photodetectors for wafer-scale characterization. a, Bird's-eye view of a NR structure, showing the Fabry–Pérot laser formed by two etched facets, the in-line photodetector on the bottom right and the common ground electrode on the bottom left. The non-functional GaAs NRs needed for fabrication and the encapsulating oxide are omitted in the drawing for clarity. Inset, cross-section HAADF-STEM image of an etched GaAs facet. **b**, 3D drawing of the wafer-scale test configuration depicting light radiated upwards by the left facet and collected by an MMF and three electrical probes driving the NR laser and monitoring the NRPD. **c**, 3D FDTD simulated electric-field intensity plot at wavelength of 1,030 nm, projected in the y–z plane, for a device with a W top contact pitch of 4.8 μm. Multimode beating is observed with a period of 4.8 μm, minimizing the optical-field intensity at the W contacts and enabling low optical propagation losses. **d**, Electric-field mode profiles at and in between the W plug locations. **e**, 3D FDTD simulation of a NR device with a dense W contact pitch of 0.3 μm, showing a rapid field decay induced by strong optical absorption loss, as in the NRPD. **f**, 3D drawing similar to **b**, showing the measurement configuration for a cleaved-facet device, with a single-mode fibre collecting the laser output and three electrical probes. Scale bar: 200 nm (**a**).

region consists of three compressively strained ($\varepsilon = -0.014$) $In_{0.2}Ga_{0.8}As$ quantum wells in the non-intentionally doped GaAs layer (Fig. 1d), and the NR is capped by an InGaP passivation layer lattice-matched to GaAs. The n-contacts of the GaAs p–i–n diodes are formed by standard CMOS Cu metallization and W plugs landing on the n^{++}-doped top surface of the silicon wafer electrically connected to the n-GaAs epitaxial layer. The p-contact is formed by a second row of W plugs, punching through the InGaP passivation layer and landing in the p^+-GaAs top contact layer. Fabrication details are reported in the Methods. To minimize loading effects and improve uniformity during epitaxy, the NR structures are grown in 1-μm pitch arrays (Fig. 1c).

A cross-sectional high-angle annular dark-field scanning transmission electron microscopy (HAADF-STEM) image with energy dispersive X-ray spectroscopy of a fabricated device is shown in Fig. 1e, and highlights the In-containing layers, the full passivation of the NRs outside the trenches by the InGaP layer, as well as the embedded InGaAs quantum wells. The HAADF-STEM image in Fig. 1f shows the full extent of the NR cross-section, revealing a well-controlled geometry from the Si-substrate to the top Cu electrode, as well as the top W contact plug piercing through the InGaP layer and landing in the p^+-GaAs layer. A close-up view of the active region dark-field (DF)-STEM in Fig. 1g shows defect-free InGaAs quantum wells and GaAs barriers, whereas a close-up view of the high aspect-ratio trench (DF-STEM, Fig. 1h) shows efficient trapping of threading dislocations at the bottom of the n-GaAs region near the silicon interface. Finally, the longitudinal HAADF-STEM image in Fig. 1i further illustrates the effective trapping of threading dislocations, which remain confined to the bottom of the ART trench. To highlight the very low TDD in NRE, we compare it with other studies on III–V-on-Si heteroepitaxy in Extended Data Table 1.

As part of the wafer-scale fabrication process, laser cavities are formed in the GaAs NRs by dry etching two facets with an angle of 12°, yielding roughly 5% facet reflectivity (Fig. 2a and Methods). On one side of the laser cavities, on-chip monitor photodetectors are formed in the same epitaxial ridges as the NRLs, whereas the other facet adjoins a larger etched area enabling out-of-plane optical emission.

A key aspect to achieve lasing in the NRs resides in optimizing the pitch of the W plugs contacting the p-GaAs layer. Efficient lasing operation is obtained for designs with a relatively large W plug pitch ($p_{con35} = 4.8$ μm). In these designs, mode beating of the fundamental TE_{00} and the higher-order TE_{01} mode results in a periodic interference pattern that minimizes the optical intensity locally underneath the W plugs (Fig. 2c,d). On the contrary, the optical field decays quickly (Fig. 2e) in the case of a tight W pitch ($p_{con35} = 0.3$ μm) because of strong absorption from the W contacts (see Methods for further discussion about p-contact optimization). Furthermore, the strong optical confinement in the NR, inferred from the two-dimensional (2D) finite-difference calculations, yields a confinement factor Γ between the three quantum wells and the optical mode as large as 8%, which is instrumental for compensating the large intracavity total optical loss at threshold (Methods).
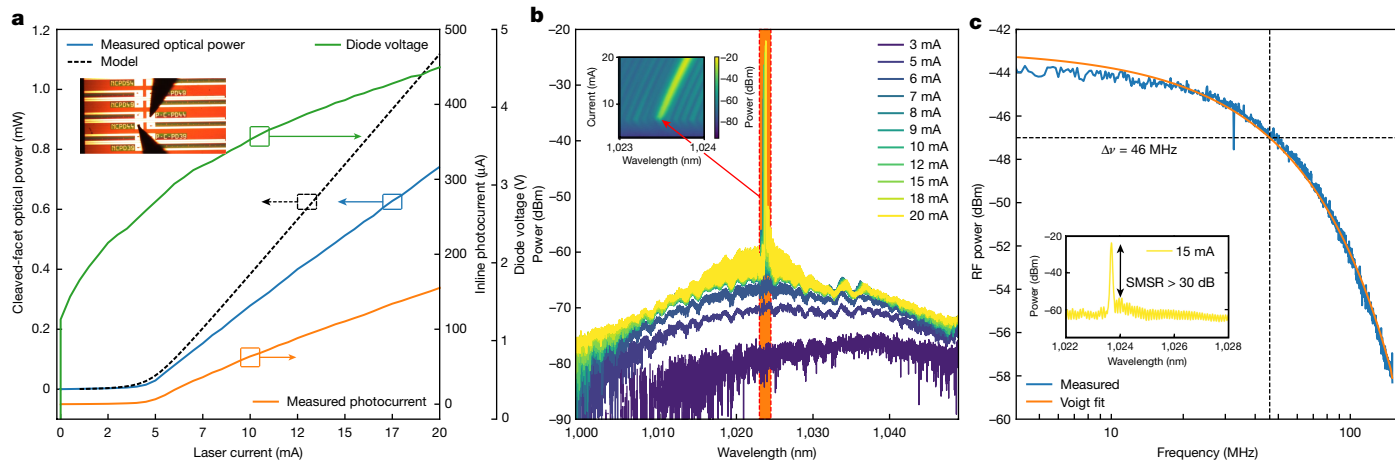
Fig. 3 | Die-level measurement of a single cleaved-facet GaAs NR laser.
a, Room-temperature L–I–V curves of a 1.16-mm-long NR laser, showing good agreement between measurements (blue solid line) and model (black dashed line), and revealing a threshold current of 4.1 mA and a single-sided slope efficiency of 0.047 W A^{-1}. The I–V curve (orange solid line) shows a diode turn-on voltage of 1.4 V. Inset, microscope image of the die-level test setup. **b**, Optical output spectra of the tested laser for bias currents ranging from

3 mA to 20 mA, showing single-mode emission across a wavelength span of 50 nm. Inset, intensity map showing single-mode mode-hopping-free lasing with a 0.4 nm redshift of the laser wavelength. **c**, Measured radiofrequency (RF) power spectrum (blue line) of the tested laser at a bias current of 15 mA, with a superimposed Voigt fit (orange line) yielding a linewidth of 46 MHz. Inset, optical output spectrum of the laser showing a SMSR exceeding 30 dB.

The test configuration used for the wafer-scale characterization of the devices is shown in Fig. 2b: three electrical probes are deployed to simultaneously bias the NRLs and the NRPDs, while a multimode fibre (MMF) optical probe is used to collect part of the upwards radiated laser emission, for subsequent power and spectral analysis. Alternatively, as depicted in Fig. 2f, one facet can be cleaved to form a mirror with roughly 40% reflectivity, while the other facet remains facing the NRPD. This configuration enables more efficient collection of the laser emission, using an edge-coupled lensed single-mode fibre, allowing for in-depth analysis of the laser performance at the die level.

Die-level laser results

First, we discuss die-level measurements to unambiguously demonstrate laser operation in the cleaved-facet GaAs NRLs. In a first measurement, we drive the NRL with a continuous-wave current at room temperature and collect the laser output from the cleaved facet by a large-area photodetector. Figure 3a shows the measured optical output power and diode voltage as a function of laser current, that is, the L–I–V (length, current and voltage) plot for a cleaved device with a cavity length of 1.16 mm. The L–I curve reveals a threshold current I_{th} as low as 4.5 mA, and a single-facet output power of up to 0.7 mW at a bias current of 20 mA. The dashed line represents the calculated L–I response, obtained by solving the laser rate equations (Methods). The model accurately predicts the measured I_{th} and is in reasonable agreement with the measured slope efficiency. The V–I curve shows a diode characteristic with turn-on voltage of 1.4 V. Above the turn-on voltage, a nonlinear V–I response can be observed, originating from the non-ohmic and relatively high contact resistance in the widely spaced contact plugs to the p-GaAs layer (Methods).

To gain extra insights into the NRLs properties, we measured a similar, 1.4-mm-long laser in a different test configuration (Fig. 2f), where the large-area photodetector is replaced with a lensed single-mode fibre connected to an optical spectrum analyser. The optical spectra recorded as a function of currents are shown in Fig. 3b, showing single-mode laser emission around 1,023 nm across a wavelength span of 50 nm. An enlargement of the same spectra (Fig. 3c) shows an I_{th} of 6 mA and a redshift of the laser wavelength up to 0.4 nm without any mode hopping with increasing drive current. To confirm that the device is indeed operating as a laser, we also carried out a linewidth

measurement using a self-homodyne setup (see Methods for further reading). From the measured radiofrequency beat note depicted in Fig. 3d, we infer a linewidth of 46 MHz at a current I_{bias} = 15 mA ($I_{bias} > 2I_{th}$). Finally, the inset in Fig. 3d illustrates a side-mode suppression ratio (SMSR) exceeding 30 dB at this current, ensuring that the radiofrequency beat note originates from a single longitudinal mode of the NRL.

Wafer-level laser results

Next, we discuss the fully wafer-scale fabricated lasers with two etched facets. As a first example, a NRL with a 2-mm-long cavity was probed on the wafer and the optical emission was measured using an on-wafer NRPD on one side and an MMF on the other side (Fig. 2b). The I–I plot depicted in Fig. 4a shows I_{th} = 7.5 mA and a maximum photocurrent of 71.5 μA at I = 17.5 mA. By considering the measured photodiode responsivity of 0.65 A.W^{-1} (ref. 46) and the simulated LD-to-PD coupling efficiency of 12.5% (Methods), we infer a total emitted power of up to 1.76 mW and a 1.33% wall-plug efficiency, which agrees well with the laser model.

As an early investigation into the reliability of the NRLs, we carried out an on-wafer stress test on one of the best performing 2-mm-long lasers. We biased the laser at 1.5I_{th} at room temperature and monitored the output power, slope efficiency and threshold current (Fig. 4c, see Methods for more information about the stress conditions). While I_{th} increased from 6.1 to 7.3 mA, the degradation showed a decelerating trend and the slope efficiency stayed largely constant. The NRL remained operational during at least 500 h of stress time, exceeding the previously reported record lifetime of 200 h for GaAs-based quantum-well lasers directly grown on silicon[47]. This device lifetime is still lower than that reported for quantum-dot lasers[28] but our current device failure is caused by the high current densities at the sparse plugs and not induced by the presence of threading dislocations.

The temperature dependence of the NRLs was investigated by mounting the tested wafer on a stage with a temperature controller and recording the L–I curves (Fig. 4b). For a 2-mm-long NRL, single-mode operation was observed at a temperature up to 55 °C, with I_{th} = 30 mA at 55 °C, compared to I_{th} = 7.5 mA at 25 °C.

To assess the reproducibility of our NR laser results, we carried out full 300-mm wafer-scale measurements using the on-wafer NRPD.
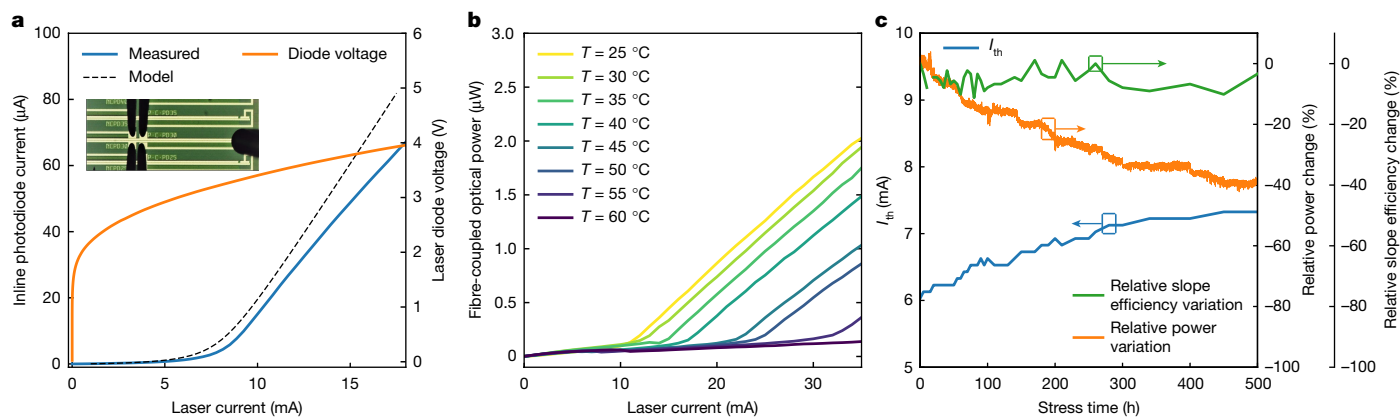
Fig. 4 | On-wafer measurement of an etched-facet GaAs NR laser. a, L–I–V curves of a 2-mm-long NR laser, showing solid agreement between the measurement (blue solid line) and the model (black dashed line), and indicating a threshold current of 7.5 mA and a slope efficiency of 6.45 μA mA^{-1} (0.25 W A^{-1}). The I–V curve (orange solid line) reveals a diode turn-on voltage of 1.5 V. Inset, microscope image of the wafer-level test configuration, showing a MMF and four electric probes. **b**, Measured fibre-coupled L–I curves of a 2-mm-long NR laser at temperatures ranging from 25 °C to 60 °C, showing continuous-wave lasing up to 55 °C (Extended Data Fig. 5). **c**, Early reliability test, showing continuous room-temperature laser operation up to 500 h at a bias current of 9.17 (1.5I_{th}) mA, with a 20% increase in threshold current, 40% relative power change at fixed bias and no significant change in the slope efficiency.

We measured three sets of NRLs with different lengths (Fig. 5a L = 1 mm, Fig. 5b L = 1.5 mm and Fig. 5c L = 2 mm) across a full wafer, gathering statistics about process variability and length dependence of the laser threshold, output power and slope efficiency (see Extended Data Fig. 6 for a full wafer map). The performance metrics of more than 300 functional NRLs were extracted and are shown in Fig. 5a–c. The calibration previously performed on single cleaved-facet NRL is used to estimate the total optical power radiated by the two facets of the lasers. Mean I_{th} values of 5.9, 8.1 and 9.3 mA were measured for 1-, 1.5- and 2-mm-long lasers, respectively (Fig. 5d). The mean slope efficiencies are 8.3, 6.1 and 4.9 μA mA^{-1}, or 0.33, 0.22 and 0.19 W A^{-1}, respectively (Fig. 5e). These measured values are in good agreement with predicted values using the laser model. The laser statistics are summarized in Extended Data Table 2.

The relatively large spread in measured threshold current, slope efficiency and output power across the wafer originates from variability in the wafer-scale processes, which have not yet been optimized for uniformity (see Methods for more information).

Discussion

This work demonstrates monolithic III–V laser diode integration on 300-mm Si wafers entirely carried out in a CMOS manufacturing pilot line, without the need for any III–V substrates or bonding steps. High-quality active GaAs waveguides are grown by MOVPE applying NRE, mitigating any major issues related to wafer bow or crack formation as typically encountered in blanket III–V layers epitaxially grown on silicon. Despite their submicrometre-scale cross-sectional dimensions,
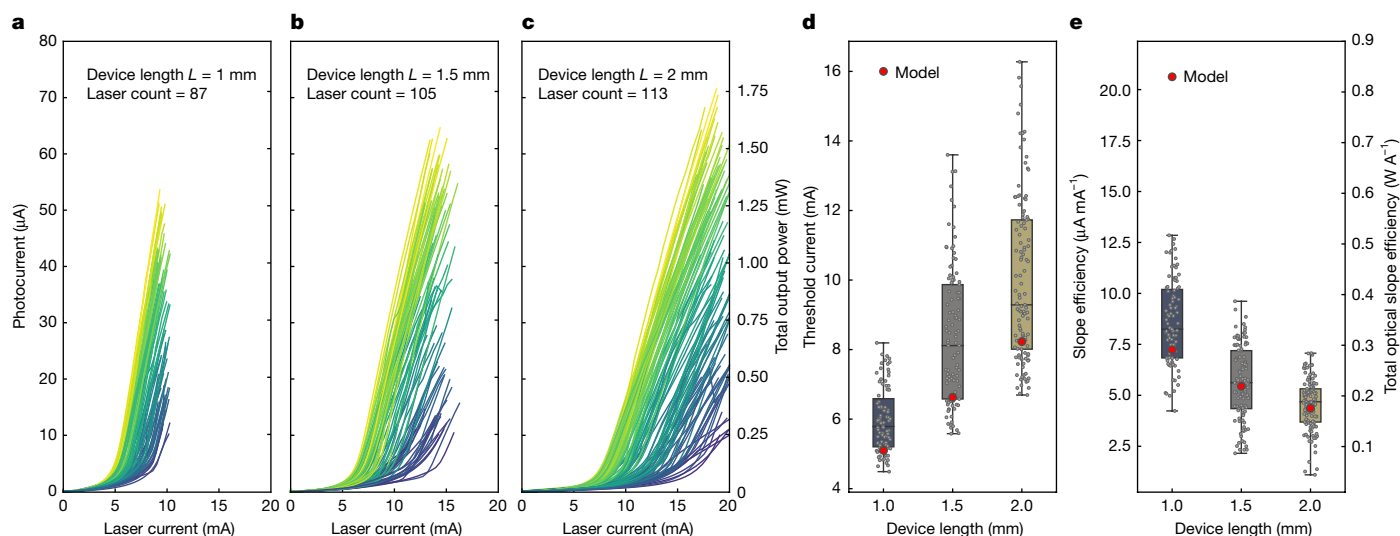

Fig. 5 | Full wafer-scale measurements of etched-facet GaAs NR lasers. a–c, I–I and L–I plots from 300 functional NR lasers using the on-wafer photodetectors for measuring laser output for 1-mm-long lasers (**a**), 1.5-mm-long lasers (**b**) and 2-mm-long lasers (**c**). The right y axis indicates the total output power radiated by the two laser facets. **d**, Measured threshold-current distribution across the measured lasers. **e**, Extracted slope efficiencies across the measured lasers. In **d** and **e**, each grey dot represents a value extracted from a single device. The red dots represent the threshold current and slope efficiency for different laser lengths as predicted by the laser rate-equation model. In the boxplots, the boxes represent the interquartile range for threshold currents and slopes efficiencies, the top and bottom edges of the boxes the first and third quartiles. The central line in the boxes represents the mean value, while the whiskers indicate the minimum and maximum values.

the GaAs–Si NR structures feature efficient carrier injection and generate strong optical gain at 1 μm wavelengths, enabled by the record-low crystal defectivity in epitaxially grown GaAs on Si and effective passivation by the InGaP capping layer. These attributes are instrumental for robust continuous-wave laser operation at room temperature and above, as demonstrated in this paper with threshold-current densities comparable with conventional laser designs and below 1 kA cm^{-2}, and continuous-wave operation up to 55 °C. In the demonstrated NRLs, an optical multimode beating effect mitigates part of the optical losses induced by the top metal contacts, which is equally essential to achieving low threshold currents and high slope efficiencies. Furthermore, the wavelength dependency of this phenomenon (Methods), together with the multi-peak spectrum originating from the Fabry–Pérot cavity formed by the etched facets, results in single-mode laser operation for most of the laser devices, with linewidths comparable or smaller than those realized in typical vertical-cavity surface-emitting lasers (Methods).

A key remaining challenge is to demonstrate the long-term reliability of the monolithic GaAs-on-Si NRLs. It is well known that quantum well-based lasers on silicon are particularly sensitive to the presence of threading dislocations, and a reliable quantum-well laser essentially needs to have a dislocation-free active region[48]. As discussed in the Methods, we estimate the TDD in our GaAs NRs to be below 6×10^4 cm^{-2} or, equivalently, on average one dislocation per 4 mm of NR length. As such, many of the tested lasers are expected to be dislocation-free, providing a positive outlook for achieving long reliability lifetimes. Several devices have indeed shown encouraging room-temperature operating lifetimes beyond 100 h, and the dominant failure mode observed so far is related to the high current density (more than 150 kA cm^{-2}) in the top metal plugs, which need to be sparsely populated to realize low optical loss in the current laser designs. An in-depth reliability analysis is continuing and will be reported elsewhere. Wafer-level uniformity of the NRs for high yield is crucial towards manufacturing. In that prospect, we have seen improvements by migrating the growth to an industrial MOVPE tool. Etching III–V materials in a CMOS foundry is another important point. Minimizing III–V material to be etched in dedicated tools is critical for waste management and redeposition during etch, and as such, our NRE enables a notable reduction of both aspects.

We see many opportunities to go beyond the current demonstration. First, the NR cross-section can be improved to decouple the optical modes from the metal contacts, enabling a much higher density of p-contact plugs while retaining low optical loss. This will lower the operating voltage and improve wall-plug efficiencies, while also reducing current density and electrical resistance in the top metal contacts, leading to improved reliability. Next, the operating wavelength can be extended towards the O-band by growing NRLs with higher In-content[49] or alternatively using InAs quantum-dots as gain material. Last, the NRLs can be optically coupled to (amorphous) silicon waveguides[50]. Coupling the GaAs NRs to silicon and silicon nitride waveguides will enable the implementation of external-cavity diode lasers, with better controlled laser wavelengths and reduced laser noise. Such a GaAs–Si–SiN integrated photonics platform is expected to enable future cost-sensitive applications in optical interconnects, optical sensing and beyond.

Online content

Any methods, additional references, Nature Portfolio reporting summaries, source data, extended data, supplementary information, acknowledgements, peer review information; details of author contributions and competing interests; and statements of data and code availability are available at https://doi.org/10.1038/s41586-024-08364-2.

1. Arrazola, J. M. et al. Quantum circuits with many photons on a programmable nanophotonic chip. *Nature* **591**, 54–60 (2021).
2. Mohanty, A. et al. Reconfigurable nanophotonic silicon probes for sub-millisecond deep-brain optical stimulation. *Nat. Biomed. Eng.* **4**, 223–231 (2020).
3. Shastri, B. J. et al. Photonics for artificial intelligence and neuromorphic computing. *Nat. Photon.* **15**, 102–114 (2021).
4. Khial, P. P. et al. Nanophotonic optical gyroscope with reciprocal sensitivity enhancement. *Nat. Photon.* **12**, 671–675 (2018).
5. Rickman, A. The commercialization of silicon photonics. *Nat. Photon.* **8**, 579–582 (2014).
6. Spencer, D. T. et al. An optical-frequency synthesizer using integrated photonics. *Nature* **557**, 81–85 (2018).
7. Nagarajan, R. et al. 2.5D heterogeneous integration for silicon photonics engines in optical transceivers. *IEEE J. Selec. Top. Quant. Electron.* **29**, 8200209 (2023).
8. Bian, Y. et al. 3D integrated laser attach technology on a 300-mm monolithic CMOS silicon photonics platform. *IEEE J. Sel. Top. Quant. Electron.* **29**, 8200519 (2023).
9. Marinins, A. et al. Wafer-scale hybrid integration of InP DFB lasers on Si photonics by flip-chip bonding with sub-300 nm alignment precision. *IEEE J. Selec. Top. Quant. Electron.* **29**, 8200311 (2023).
10. Ramirez, J. M. et al. III-V-on-silicon integration: from hybrid devices to heterogeneous photonic integrated circuits. *IEEE J. Selec. Top. Quant. Electron.* **26**, 6100213 (2020).
11. Fujii, T. et al. Multiwavelength membrane laser array using selective area growth on directly bonded InP on SiO2/Si. *Optica* **7**, 838–846 (2020).
12. Xiang, C. et al. Narrow-linewidth III-V/Si/Si3N4 laser using multilayer heterogeneous integration. *Optica* **7**, 20–21 (2020).
13. Margalit, N. et al. Perspective on the future of silicon photonics and electronics. *Appl. Phys. Lett.* **118**, 220501 (2021).
14. Zhang, W. et al. Silicon photonic integrated optoelectronic oscillator for frequency-tunable microwave generation. *J. Lightwav. Technol.* **36**, 4655–4663 (2018).
15. Wang, J. et al. Multidimensional quantum entanglement with large-scale integrated optics. *Science* **360**, 285–291 (2018).
16. Fotiadis, K. et al. Silicon photonic 16 x 16 cyclic AWGR for DWDM O-band interconnects. *IEEE Photon. Technol. Lett.* **32**, 1233–1236 (2020).
17. Khani, M. et al. SiP-ML: high-bandwidth optical network interconnects for machine learning training. In *Proc. ACM Special Interest Group on Data Communication Conference* 657–675 (ACM, 2021).
18. Coomans, W. et al. XG-fast: the 5th generation broadband. *IEEE Commun. Mag.* **53**, 83–88 (2015).
19. Driscoll, J. B., Perea, P., Kauffman, A., Zilkie, A. J. & Ver Steeg, B. Pioneering silicon photonics for wearable sensors. In *Proc. Optical Fiber Communications Conference and Exhibition (OFC) 2023* Th1A.6 1–3 (Optica Publishing Group, 2023).
20. De Dobbelaere, P. et al. Packaging of silicon photonics systems. In *Proc. Optical Fiber Communication Conference (OFC) 2014* W3I.2 1–3 (Optica Publishing Group, 2014).
21. Roelkens, G. et al. Present and future of micro-transfer printing for heterogeneous photonic integrated circuits. *APL Photon.* **9**, 010901 (2024).
22. Intel. Intel Labs announces integrated photonics research advancement. *Intel Newsroom* https://www.intel.com/content/www/us/en/newsroom/news/intel-labs-announces-integrated-photonics-research-advancement.html (2022).
23. Tower Semiconductor. Tower Semiconductor announces World's first heterogeneous integration of quantum dot lasers on its popular SiPho foundry platform PH18. *Press Releases* https://towersemi.com/2023/03/02/03022023/ (2023).
24. Shi, B. et al. MOCVD grown low dislocation density GaAs-on-V-groove patterned (001) Si for 1.3 μm quantum dot laser applications. *Appl. Phys. Lett.* **114**, 172102 (2019).
25. Chen, S. et al. Electrically pumped continuous-wave III–V quantum dot lasers on silicon. *Nat. Photon.* **10**, 307–311 (2016).
26. Wan, Y. et al. InAs/GaAs quantum dots on GaAs-on-V-grooved-Si substrate with high optical quality in the 1.3 μm band. *Appl. Phys. Lett.* **107**, 081106 (2015).
27. Liu, A. Y. et al. Reliability of InAs/GaAs quantum dot lasers epitaxially grown on silicon. *IEEE J. Selec. Top. Quant. Electron.* **21**, 690–697 (2015).
28. Shang, C. et al. High-temperature reliable quantum-dot lasers on Si with misfit and threading dislocation filters. *Optica* **8**, 749–754 (2021).
29. Shang, C. et al. Electrically pumped quantum-dot lasers grown on 300 mm patterned Si photonic wafers. *Light: Sci. Appl.* **11**, 299 (2022).
30. Wei, W.-Q. et al. Monolithic integration of embedded III-V lasers on SOI. *Light Sci. Appl.* **12**, 84 (2023).
31. Fiorenza, J. G. et al. Aspect ratio trapping: a unique technology for integrating Ge and III-Vs with silicon CMOS. *ECS Trans.* **33**, 963 (2010).
32. Li, J. Z. et al. Defect reduction of GaAs epitaxy on Si (001) using selective aspect ratio trapping. *Appl. Phys. Lett.* **91**, 021114 (2007).
33. Waldron, N. et al. Integration of InGaAs channel n-MOS devices on 200 mm Si wafers using the aspect-ratio-trapping technique. *ECS Trans.* **45**, 115 (2012).
34. Wen, P. et al. Waveguide coupled III-V photodiodes monolithically integrated on Si. *Nat. Commun.* **13**, 909 (2022).
35. Han, Y. et al. Selective lateral epitaxy of dislocation-free InP on silicon-on-insulator. *Appl. Phys. Lett.* **114**, 192105 (2019).
36. Xue, Y. et al. High-speed and low dark current silicon-waveguide-coupled III-V photodetectors selectively grown on SOI. *Optica* **11**, 1219–1226 (2022).
37. Kunert, B. et al. III/V nano ridge structures for optical applications on patterned 300 mm silicon substrate. *Appl. Phys. Lett.* **109**, 091101 (2016).
38. Kunert, B. et al. Integration of III/V hetero-structures by selective area growth on Si for nano- and optoelectronics. *ECS Trans.* **75**, 409 (2016).
39. Kunert, B. et al. How to control defect formation in monolithic III/V hetero-epitaxy on (100) Si? A critical review on current approaches. *Semicon. Sci. Technol.* **33**, 093002 (2018).
40. Baryshnikova, M. et al. Nano-ridge engineering of GaSb for the integration of InAs/GaSb heterostructures on 300 mm (001) Si. *Crystals* **4**, 330 (2020).
41. Kunert, B. et al. Application of an Sb surfactant in InGaAs nano-ridge engineering on 300 mm silicon substrates. *Crystal Growth Design* **21**, 1657–1665 (2021).
42. Van Thourhout, D. et al. *Semiconductors and Semimetals* Ch. 8 (Elsevier, 2019).
43. Mols, Y. et al. Structural analysis and resistivity measurements of InAs and GaSb fins on 300 mm Si for vertical (T)FET. *J. Appl. Phys.* **125**, 245107 (2019).

44. Shi, Y. et al. Optical pumped InGaAs/GaAs nano-ridge laser epitaxially grown on a standard 300-mm Si wafer. *Optica* **12**, 1468–1473 (2017).

45. Vais, A. et al. First demonstration of III-V HBTs on 300 mm Si substrates using nano-ridge engineering. In *Proc. International Electron Devices Meeting (IEDM)* 9.1.1–9.1.4 (IEEE, 2019).

46. Özdemir, C. I. et al. Low dark current and high responsivity 1020 nm InGaAs/GaAs nano-ridge waveguide photodetector monolithically integrated on a 300-mm Si wafer. *J. Lightwav. Technol*. **39**, 5263–5269 (2021).

47. Kazi, Z. I. et al. Realization of GaAs/AlGaAs lasers on Si substrates using epitaxial lateral overgrowth by metalorganic chemical vapor deposition. *Jpn J. Appl. Phys*. **40**, 4903 (2001).

48. Hasegawa, Y., Egawa, T., Jimbo, T. & Umeno, M. Influences of dark line defects on characteristics of AlGaAs/GaAs quantum well lasers grown on Si substrates. *Jpn J. Appl. Phys*. **34**, 2994 (1995).

49. Colucci, D. et al. Unique design approach to realize an O-band laser monolithically integrated on 300 mm Si substrate by nano-ridge engineering. *Opt. Express* **30**, 13510–13521 (2022).

50. Shi, Y. et al. Novel adiabatic coupler for III-V nano-ridge laser grown on a Si photonics platform. *Opt. Express* **27**, 37781–37794 (2019).

Article

Methods

Device fabrication

The devices are processed on 300-mm silicon wafers with a {001} orientation, starting with the formation of 300-nm tall Si ridges and subsequent oxide deposition and planarization following a standard shallow trench isolation process typical in CMOS foundries, and n-type ion implantation of Si. The Si ridges are subsequently wet etched using tetramethylammonium hydroxide to form V-shaped trenches in the shallow trench isolation oxide, with two {111} facets used as the starting surface for subsequent III–V epitaxy. GaAs p–i–n NRs containing three $In_{0.2}Ga_{0.8}As$ quantum wells and capped by an $In_{0.5}Ga_{0.5}P$ passivation layer are grown in one process step using MOVPE. The Si wafers are then coated with oxide and planarized. Laser mirrors and photodiode facets are subsequently patterned using deep-ultraviolet lithography and III–V dry etch. Next, the wafers are again coated with oxide and planarized. Subsequently, the fabrication steps move to back-end of line processing to form W contact plugs to the p-GaAs and n-Si contact layers. Final metallization is done using a standard CMOS Cu Damascene process. The high-level process flow of the wafer-level manufacturing of the GaAs NR lasers on Si is depicted in Extended Data Fig. 1.

Epitaxy and crystal defects

NR engineering of the III–V NRs on trench-patterned Si was carried out by MOVPE in a 300-mm deposition chamber applying tertiarybutyl arsine (TBAs), tertiarybutyl phosphine (TBP), trimethyl arsine (TMAs), triethylgallium (TEGa), trimethylgallium (TMGa) and trimethylindium (TMIn) as group-V and -III precursors, respectively. Silane (SiH_4) and carbon tetrabromide (CBr_4) were used to achieve n- and p-doped layers. Before the III–V deposition, the patterned Si wafers were loaded into an Siconi chamber from Applied Materials for the native oxide removal from the {111} Si surfaces at the trench bottom at temperatures below 200 °C. The GaAs nucleation was done at 360 °C applying TEGa before the growth temperature was raised to 590 °C for the n-doped GaAs (roughly 5×10^{18} cm^{-3}) trench filling and first n-doped box formation using TMGa. The undoped InGaAs–GaAs multi-quantum well stack was deposited at 570 °C and the TMIn/TMGa+TMIn ratio was adjusted to achieve an In concentration of about 21% inside the quantum wells. The p- and p$^+$-doped GaAs layers (roughly 1×10^{19} and 5×10^{19} cm^{-3}) were grown at 580 and 550 °C, respectively, and the InGaP layer added at high growth temperature again. The TBAs/III, TMAs/III and TBP/III ratios were varied between 4 and 60 as a function of the material, doping and growth temperature.

The threading dislocation and planar defect densities of the GaAs NR were investigated before and reported in refs. 40,51 by electron channelling contrast imaging. Especially for narrow trenches (less than 120 nm), the misfit defect density was so low that our electron channelling contrast imaging investigation did not provide sufficient defect statistics. To explore a larger sample area, we applied cathodoluminescence on a cleaved wafer piece at 77 K to reduce carrier mobility. The inspected die area was chosen at a wafer radius of about 75 mm. Ten images were acquired in which each image covered about 60 NRs with a length of 64 μm to achieve good defect statistics. Extended Data Fig. 2 shows a representative image pair: Extended Data Fig. 2a is the standard top-view scanning electron microscopy image to identify any NR line cuts and/or surface particles and Extended Data Fig. 2b the corresponding cathodoluminescence image integrated over the complete emission spectra. A dark spot in cathodoluminescence can be caused by the presence of a threading dislocation but also by any NR line cut or particle. In this investigation, the defect character could not be distinguished, but every indication of a dark spot was considered as a defect. This led to a final defect density based on this first cathodoluminescence investigation of 6×10^4 cm^{-2}. Planar defects such as micro-twins and stacking faults lie in a crystallographic plane perpendicular to the trench line. They penetrate the complete NR

volume and always reach the NR surface. However, they do not cause any dark spot in cathodoluminescence of NRs. This is caused by the fact that no partial dislocation, always present at the end of a planar defect, remains inside the NR volume as it would be the case for a planar defect in a blanket two-dimensional layer. This conclusion is also supported by the observation that the planar defect density of the GaAs NRs, which is in the range of 0.1–0.5 μm^{-1} (defect per micrometre NR length) (ref. 40), is much higher than the extracted dark spot density in CL.

We compare our work to other publications in Extended Data Table 1, and we show more than two orders of magnitude reduction in defect density on a 300-mm wafer, while enabling a significant decrease in III–V thickness thanks to the suppression of the need for III–V buffer layers. The record-low TDD value is crucial in enabling continuous-wave operation in an electrically pumped quantum-well laser on silicon.

W plug pitch optimization and confinement factor

For dense contact pitch designs, the strong spatial overlap between the optical mode propagating in the GaAs NR waveguide and the W plugs induces very large optical losses that prohibit lasing. Yet, efficient lasing operation is obtained for laser designs with a relatively large W plug pitch ($p_{con35} = 4.8$ μm). In these designs, mode beating of the fundamental TE_{00} and the higher-order TE_{01} mode results in a periodic interference pattern that minimizes the optical intensity locally underneath the W plugs, as illustrated by the simulated mode profiles shown in Fig. 2c,d. This mode-beating behaviour enables low-loss optical propagation through the NRL structure (Fig. 2c), whereas in the case of a tighter W pitch (Fig. 2e) ($p_{con35} = 0.3$ μm), the optical field decays quickly because of the strong absorption from the W contacts. The reduction of the optical loss through mode-beating engineering is detailed in the next section.

The strong optical confinement in the NR, inferred from the 2D finite-difference simulations using Ansys Lumerical software (Extended Data Table 3 and Extended Data Fig. 3d,e), yields a confinement factor Γ between the three quantum wells and the optical mode as large as 8%, which is instrumental for compensating the large intracavity total optical loss at threshold:

$$\Gamma g_{th} = \alpha_i + \alpha_m \qquad (1)$$

where g_{th} is threshold gain, α_i is the laser internal and α_m is the total mirror loss.

Optical loss

The intracavity photon loss rate γ_p is a key attribute driving laser performance. A high mirror loss rate $v_g \alpha_m$ is desired to maximize the output power and wall-plug efficiency through a large slope efficiency η_d but competes with the need to have a small intracavity photon loss rate γ_p to minimize the threshold current, as the total intracavity loss can in some cases exceeds the maximum achievable modal gain, preventing lasing operation. In the demonstrated NR lasers, the presence of W vias in the vicinity of the active region induces optical scattering and absorption. These vias pierce through the InGaP passivation layer and land on the p-doped GaAs layer to form the anode. The arrangement of these W plugs with respect to the NR waveguide has been carefully optimized.

Extended Data Fig. 6a shows the optical loss spectrum for a one-dimensional array of W contact plugs with 105 nm plug diameter and 300 nm plug pitch (35% fill factor) in blue, similarly to the case depicted in Fig. 2e in the main text. The loss spectrum is calculated using three-dimensional (3D) finite-difference time-domain (FDTD) simulations (Ansys Lumerical software) by launching the fundamental TE mode into the laser waveguide and observing the transmission through a segment of fixed length with tungsten plugs. The resulting optical loss is relatively flat across wavelength and is as high as 1,200 cm^{-1}. Such a

high loss number cannot be compensated by the gain from the quantum wells and therefore prevents the device from lasing. We observe that the propagating light quicky decays as shown in Extended Data Fig. 6b (also shown in Fig. 2e from the main text). The absorption loss can be minimized by reducing the plug density. By increasing the pitch from 0.3 to 4.8 μm while keeping the plug diameter fixed at 105 nm, the plug density is reduced by a factor of 16, which should result in a similar decrease in optical loss. Extended Data Fig. 6a shows the simulated loss spectrum by 3D FDTD for this configuration in orange. As expected, the baseline loss decreases by roughly a factor of 16 from 1,200 down to 75 cm^{-1} (dashed blue line). However, the loss spectrum is no longer flat but shows several dips where the optical loss reaches values as low as 19 cm^{-1} at a dip wavelength near 1,045 nm, where the peak gain value of the InGaAs quantum wells is located.

To understand the nature of these low-loss dips, we have investigated light propagation through the NR waveguide structure. First, we consider the NR waveguide without the tungsten contact plugs. This waveguide supports several eigenmodes as shown in Extended Data Table 3 at a wavelength of 1,050 nm. When we inspect the field profile from the 3D FDTD simulation with 4.8 μm plug pitch at 815 and 1,045 nm, we observe beating patterns with periods of 4.8 and 2.4 μm for the TE$_{00}$ + TE$_{01}$ (Extended Data Fig. 3c) and TE$_{00}$ + TE$_{02}$ (Extended Data Fig. 3f) modes, respectively. The CON35 pitch (p_{con35}) is a multiple of the beating period and the field profile is aligned in such a way that there is minimal interaction between the optical field and the tungsten plug, resulting in low optical loss. A cross-section of the field profile at two locations (at the W plug, Extended Data Fig. 3d,g, and between two W plugs, Extended Data Fig. 3e,h) reveals that the field is pushed down below the W plug for these two wavelengths. These two wavelengths correspond to dips in the loss spectrum.

The engineering of the interference patterns between these two modes through the optimization of the p-contact pitch is crucial to reduce the internal loss to a level that enables to reach threshold. As we have seen, setting the p_{con35} to 4.8 μm in our case allows reducing the optical loss down to 19 cm^{-1}.

Mirror reflectivity

The mirror reflectivity at the cleaved facet is calculated with 3D FDTD (Ansys Lumerical software). We consider normal incidence of the fundamental TE$_{00}$ mode at the NR–air interface (Extended Data Fig. 4a). We get the transmission and reflection spectra shown in Extended Data Fig. 4b, yielding 45 and 35% at the wavelength range of interest (near 1,020 nm). Finally, the far-field radiation pattern is depicted in Extended Data Fig. 4c, showing a strong beam divergence along the horizontal axis.

To assess the impact of the etched-facet angle, 3D FDTD simulations were also carried out. As this etched facet forms the second mirror of the NR laser cavity, it is essential to evaluate the influence of the sidewall angle on the mirror reflection and transmission. This is also important for estimating the amount of power coupled to the in-line photodiode (PD) and radiated vertically for light collection with a MMF. We consider an etched area filled with oxide along the NR axis characterized by its sidewall angle φ, its depth D and its length L (Extended Data Fig. 4d). In the simulation cell, three monitors are placed such as to detect the reflected power by the etched facet, the transmitted power through the in-line photodiode facet and the power scattered upwards and collected by an MMF. An inset showing a cross-sectional HAADF-STEM image of the etched facet (Extended Data Fig. 4d) indicates that for our fabricated devices, the sidewall angle is 12° whereas the etch depth is 1,000 nm. The simulation results are depicted in Extended Data Fig. 5e–h.

We estimate from the laser rate-equation model that a minimum reflection of 2.5% is required to reach threshold (dashed line in Extended Data Fig. 4e,f). We observe that for our etched facets, the reflection is roughly 5% when L is 4 μm (Extended Data Fig. 4e) and 1 μm

(Extended Data Fig. 4f). The transmission into the in-line photodiode is estimated to be around roughly 12.5% (Extended Data Fig. 4g), whereas roughly 1% of the power is scattered upwards (Extended Data Fig. 4h). This estimation enables to correlate the collected photocurrent with the total emitted power from the NR laser.

Laser modelling

The mode profile, field overlap with the quantum wells and total internal loss were simulated considering the dimensions of fabricated NR devices, using the 2D finite-difference method with Ansys Lumerical software. Optimization of the W plug pitch to minimize propagation loss, and estimation of etched mirror reflectivity and fibre collection efficiency was carried out using 3D FDTD simulations in Ansys Lumerical software. The electrical injection efficiency and carrier loss rates were simulated using the technology computer-assisted design (TCAD) Poisson solver in the Synopsis Sentaurus software. Finally, the laser threshold current and slope efficiency were computed using Python-based codes solving the standard laser rate equations, enabling us to correlate the simulated parameters with the measured data. We express the general form of these equations as in ref. 52:

$$\frac{dN}{dt} = \frac{\eta_i I}{qV_a} - AN - BN^2 - CN^3 - v_g g_0 \log\left(\frac{N}{N_{tr}}\right)N_p \qquad (2)$$

$$\frac{dN_p}{dt} = \left(\Gamma v_g g_0 \log\left(\frac{N}{N_{tr}}\right) - \gamma_p\right)N_p + \Gamma\beta BN^2, \qquad (3)$$

where N and N_p are the carrier and photon densities, η_i is the carrier injection efficiency extracted from the TCAD simulation, I is the injected current, q is the electron charge and V_a is the active volume. A, B and C are the Schockley–Read–Hall recombination, the bimolecular recombination and the Auger coefficients, respectively. v_g is the group velocity, g_0 the gain coefficient and N_{tr} the transparency carrier density. Γ is the confinement factor, that is, the fraction of the optical mode confined in the quantum wells, γ_p is the cavity photon loss rate and β is the spontaneous emission factor. Recalling that the laser is at threshold when the modal gain exactly compensates the total loss of the laser, we recover the threshold modal gain from equation (1). This allows us to readily express the threshold carrier density:

$$N_{th} = N_{tr} \exp\left(\frac{\alpha_i + \alpha_m}{\Gamma g_0}\right) \qquad (4)$$

Because we are operating our lasers in continuous wave, we can reduce the rate equations to the steady-state case. As no stimulated emission occurs at threshold, we get:

$$0 = \frac{\eta_i I_{th}}{qV_a} - AN_{th} - BN_{th}^2 - CN_{th}^3 \qquad (5)$$

$$0 = -\gamma_p N_p + \Gamma\beta BN^2 \qquad (6)$$

We finally obtain the threshold current value:

$$I_{th} = \frac{qV_a}{\eta_i}(AN_{th} + BN_{th}^2 + CN_{th}^3) \qquad (7)$$

As the gain is clamped at threshold, we can express above threshold the steady-state carrier density rate equation:

$$\frac{\eta_i I}{qV_a} - \frac{qV_a}{\eta_i}(AN_{th} + BN_{th}^2 + CN_{th}^3) - v_g g_{th} N_p = 0 \qquad (8)$$

With appropriate substitutions, we have:

$$\upsilon_g g_{th} N_p = \frac{\eta_i I}{q V_a} - \frac{\eta_i I_{th}}{q V_a} \tag{9}$$

We get the linear relationship between intracavity photon density and the injected current:

$$N_p = \frac{\eta_i}{q V_a \upsilon_g g_{th}} (I - I_{th}) \tag{10}$$

To obtain the total output power, we can readily express the energy stored in the cavity:

$$E_{cav} = \hbar\omega N_p \frac{V_a}{\Gamma} \tag{11}$$

The total output power corresponds to the energy loss rate through the mirrors, that is:

$$P_{out} = \upsilon_g \alpha_m E_{cav} \tag{12}$$

By applying the appropriate substitutions, we get:

$$P_{out} = \frac{\eta_i \alpha_m}{\alpha_i + \alpha_m} \frac{\hbar\omega}{q} (I - I_{th}) = \eta_i \eta_{opt} \frac{\hbar\omega}{q} (I - I_{th}) \tag{13}$$

where $\eta_{opt} = \alpha_m/(\alpha_m + \alpha_i)$ is the slope efficiency. The output power per facet can be expressed by adding a coefficient $F_{1(2)}$ derived from the facet reflectivity $r_{1(2)}$ and transmittivity $t_{1(2)}$:

$$F_{1(2)} = \frac{t_{1(2)}^2}{(1 - r_{1(2)}^2) + \frac{r_{1(2)}}{r_{2(1)}}(1 - r_{2(1)}^2)} \tag{14}$$

The expression of $F_{1(2)}$ also accounts for lossy mirrors when $r_{1(2)}^2 + t_{1(2)}^2 < 1$. We can therefore relate the measured output power at each facet $P_{1(2)}$:

$$P_{1(2)} = F_{1(2)} \eta_i \eta_{opt} \frac{\hbar\omega}{q} (I - I_{th}) \tag{15}$$

The different parameters and their respective values are detailed in Extended Data Table 4 and in refs. 53,54.

Die-level measurements

The characterized devices were taken from a fully processed 300-mm wafer cleaved into smaller dies. A high-precision cleaving tool was used to form a mirror in the middle of the NR structure. The lasers were then characterized on a die-level probing setup using a large-area photodiode to extract the single-facet output power, while the light emitted from the other etched facet was collected by the in-line photodiode. Spectral analysis of the laser emission was carried out by collecting the emitted light using an edge-coupled lensed fibre connected to an optical spectrum analyser.

Estimation of total laser output power

The die-level measurement configuration allows an estimation of the total optical power radiated by both facets. Let us note the output powers at the cleaved facet and the etched facet to be P_1 and P_2, and their respective transmission coefficients t_1 and t_2. t_1 and t_2 are calculated through 3D FDTD simulations (Extended Data Fig. 4) and are evaluated to be $t_1 = 0.45$ and $t_2 = 0.30$, respectively. 3D FDTD simulation is also used to estimate the coupling efficiency of the laser diode into the monitor photodetector (PD), yielding $t_{laser \to PD} = 12.5\%$. This value

accounts for the reflection at the PD facet, the beam diffraction at the laser facet and the beam divergence in the etched gap between the two devices. Knowing the photodiode responsivity $R_{PD} = 0.65$ A W^{-1} (ref. 46), the measured optical power on the cleaved-facet side is related to the measured photocurrent on the etched-facet side as:

$$I_{PD} = \frac{t_2}{t_1} R_{PD} t_{laser \to PD} P_1 \tag{16}$$

We can extend this relationship to the wafer-level measurement case, where both facets have equal transmission and reflection (that is, $t_1 = t_2 = t$ and $P_1 = P_2 = P$), which reduces the relationship to:

$$I_{PD} = R_{PD} t_{laser \to PD} P \tag{17}$$

Finally, we can express the total output power of the NR laser from the photocurrent readout, as depicted in Fig. 5a–c:

$$P_{tot} = 2 \frac{I_{PD}}{R_{PD} t_{laser \to PD}} \tag{18}$$

Wafer-level and reliability measurements

Wafer-scale laser characterization was carried out using a 300-mm semi-automated wafer probe station fitted out with a temperature controller and a MMF to collect the laser emission, enabling the measurement of thousands of devices on a single wafer at high throughput. Temperature-dependent measurements were performed on the wafer level, and Extended Data Fig. 5 depicts the results obtained on one of the best performing 2-mm-long laser. Temperature ranges from 25 to 60 °C, and both L–I curves (Extended Data Fig. 5a) and optical spectra (Extended Data Fig. 5d) show laser operation up to 55 °C. Fitting temperature-dependent threshold current and slope efficiency yields characteristic temperatures $T_1 = 29$ K and $T_2 = 94.9$ K, respectively (Extended Data Fig. 5b,c). Extended Data Fig. 5d indicates that the laser is at threshold when $T = 60$ °C. A linear fit of the laser wavelength as a function of the temperature yields a redshift of 71.1 pm K^{-1} (Extended Data Fig. 5e). In addition, a fit of the current-dependent laser wavelength yields a slope of 13.6 pm mA^{-1} (Extended Data Fig. 5f,g).

Early reliability measurements were carried out using the same setup, tracking the performance of one of the best performing NRLs during a 500-h-long stress test. In this test, the laser bias current was kept at 9.17 mA (of 1.5I_{th}) and the wafer stage was kept at 25 °C. Bias current sweeps were carried out every 20 h, and L–I plots were recorded to extract threshold current, output power and slope efficiency.

Wafer-level variability

We identified several factors that account for wafer-level variability. First, variations in the GaAs NR width and height across the 300-mm wafer originating from the MOVPE process variability induce changes in the confinement factor Γ within the InGaAs quantum wells, as well as in the mode-beating periodicity, which in turn increases the absorption loss from the metal contact. Second, wafer-scale variation of the InGaP–GaAs etch process needed to land the W vias on the p-GaAs layer and residual topography after the planarization steps required for the back-end of line processing may lead to shorted or open-circuit electrodes. On the other hand, no significant effect resulting from quantum-well thickness variation across the wafer was observed. This effect is negligible compared to the NR dimension variations that are inducing a significantly larger wavelength shift. The lowest threshold current values are found mostly in a ring-like shape at half the diameter of the 300-mm wafer. We note that these values are obtained after binning of the tested devices (more than 1,300 in total), resulting in the removal of the dies at the edge of the wafer that contained only

light-emitting diodes or short circuits, owing to the failure modes described above. The wafer-scale variability is further illustrated in Extended Data Fig. 6a,b, which depicts the distribution of the threshold current and slope efficiency of all the tested devices across the wafer. Roughly, Extended Data Fig. 6c shows the lasing wavelength distribution across the wafer from eight identical 2-mm-long lasers biased at a current of 35 mA, showing a lasing wavelength ranging from 1,023.59 to 1,037.83 nm, which is smaller than the gain spectrum.

Laser linewidth measurements
The self-homodyne interferometric setup used to measure the laser linewidth of various devices is depicted in Extended Data Fig. 7a. The device under test (DUT), a NRL with a cleaved facet, is electrically probed by DC needles connected to a Keithley current source. A current compliance is set to 20 mA to prevent from damaging the laser diode. The laser light is collected at the cleaved facet forming one of the laser cavity mirrors by a lensed fibre. This fibre is connected to a fibred Mach–Zehnder interferometer containing a polarization controller in one arm and a 1-km-long fibre delay line in the other arm. The combined signal from the two arms is collected by a balanced photodiode (400-MHz balanced photodetector Thorlabs PDB471C-AC) and the electrical readout signal is sent to an Electrical Spectrum Analyzer (Rhode & Schwartz 100 Hz–13 GHz), enabling extraction of the laser phase noise. No acousto-optic modulator is used in the setup to offset the frequency owing to the lack of an available acousto-optic modulator in the laser wavelength range (roughly 1,030 nm) in our setup. No optical isolator is placed in front of the DUT, making the laser unshielded from parasitic reflections and yielding to an overestimate of the laser linewidth. In addition to the electrical power spectral density shown in the main text (Fig. 3c), electrical power spectra of ten more devices are shown in Extended Data Fig. 7b. The radiofrequency power spectra of the measured beat notes are measured at bias currents of 15 and 18 mA, that is, greater than $2I_{th}$. The linewidths extracted using a Voigt fit range from 46 MHz for the best device (shown in the main text) up to 186 MHz and are depicted in Extended Data Fig. 7b.

The difference in linewidths is manifold: (1) the laser performance is affected by NR shape variability across the wafer, affecting the threshold current, the slope and the SMSR. (2) Laser performance depends on the interaction of many optical modes, which in turn depends on the (varying) NR laser dimensions (Fabry–Pérot cavity design with transverse mode beating, trench width design for ART, p-contact W plug pitch design). (3) The laser is not shielded from optical feedback with an optical isolator. (4) The laser operates at a moderate bias current (roughly $2I_{th}$) to prevent laser failure. (5) No active stabilization besides temperature control is applied to the DUT. Nonetheless, the measured linewidths place our NR lasers between commercial distributed feedback lasers (less than or equal to 1 MHz) and vertical-cavity surface emission lasers (more than 1 GHz) (ref. 55). More importantly, these measurements confirm that our NR devices are lasing and are not in an amplified spontaneous regime. Finally, we compare the measured linewidths with the theoretical expression of the modified Schawlow–Townes linewidth (ref. 56):

$$\Delta\nu_{ST} = \frac{\hbar\omega\nu_g\Gamma g_{th}n_{sp}\alpha_m}{8\pi\eta_{opt}P_{out}}(1+\alpha^2),\tag{19}$$

where n_{sp} is the population inversion factor, typically around 1.25–1.75, and α is the well-known linewidth enhancement factor, typically around 4–6 for quantum-well lasers. By assuming $n_{sp}=1.5$ and $\alpha=4.5$, and by setting the total output power of one of our NR lasers to 2.3 mW (for a cleaved-facet output power of 0.5 mW), we get $\Delta\nu_{ST}=30$ MHz, which is in line with the best measured linewidth ($\Delta\nu_{ST}=46$ MHz) among the devices that were tested (Extended Data Fig. 7b).

We expect to strongly reduce the laser linewidth in future designs by suppressing the beating modes, by improving the p-contact scheme allowing to operate at much larger currents and by introducing a distributed feedback grating in the NR devices to reduce α_m. Future experiments will expand the laser characterization to include relative intensity noise measurements and extend the bias current range to larger values to observe a reduction of the Schawlow–Townes linewidth.

Spontaneous emission factor
We extract the spontaneous emission factor β from the I–I curve of one of our lasers and we fit it with the laser rate-equation model. From the Extended Data Fig. 8, we infer a β as large as 1.5×10^{-2}. We attribute this large β to the fact that the NR lasers operate below threshold as a superluminescent light-emitting diode (ref. 57) because of the low mirror reflectivity (5%) and the strong optical confinement.

GaAs–Si diode resistance
As noted in the main text, the laser diodes have a relatively large operating voltage of 3–4 V (Extended Data Fig. 9a). To assess the origin of this large diode voltage, we compare the J–V characteristics (current density versus diode voltage) of several laser diodes ($p_{con35}=4.8$ µm) with photodetectors ($p_{con35}=0.3$ µm), suspecting the sparsity of the W plug contacting the p-GaAs (that is, a large contact pitch p_{con35}) as a main contributor to high device resistance. As shown in Extended Data Fig. 9a, a voltage of roughly 3.5 V enables a current density of roughly 1 kA cm^{-2} when $p_{con35}=4.8$ µm, while in the case of $p_{con35}=0.3$ µm, it enables a much higher current density of 3–4 kA cm^{-2}. From the J–V characteristics, we extract the associated series resistances at a voltage of 4 V for the two configurations. We infer a mean series resistance of 57 Ω mm^{-1} for $p_{con35}=0.3$ µm and 115 Ω mm^{-1} for $p_{con35}=4.8$ µm, showing a twofold increase as shown in the box plots in Extended Data Fig. 9b.

Whereas a p_{con35} of 4.8 µm is key in achieving lasing through mode beating minimizing optical loss below the W plug in our current designs, we see room for improving the laser diode operating voltage and resistance in future designs by moving the W plugs away from the active region and increasing the W plug density, which will also positively affect the laser reliability. Furthermore, increasing the doping level in the p-type GaAs contact layer will help to realize ohmic contacts to further reduce the operating voltage and improve wall-plug efficiency (ref. 58).

Reporting summary
Further information on research design is available in the Nature Portfolio Reporting Summary linked to this article.

Data availability
The measured and presented datasets in this study are available via Zenodo at https://doi.org/10.5281/zenodo.13286360 (ref. 59). Source data are provided with this paper.

Code availability
The evaluation scripts and models used in this study are available via Zenodo at https://doi.org/10.5281/zenodo.13286360 (ref. 59).

51. Kunert, B. et al. How to control defect formation in monolithic III/V heteroepitaxy on (100) Si? A critical review on current approaches. *Semiconductor Sci. Technol.* **33**, 093002 (2018).
52. Coldren, L. A. et al. *Diode Lasers and Integrated Circuits* (Wiley, 2012).
53. Strand, T. A. et al. Low regrowth-interface recombination rates in InGaAs-GaAs buried ridge lasers fabricated by in situ processing. *Appl. Phys. Lett.* **66**, 1966–1968 (1995).
54. Tsvid, G. et al. Spontaneous radiative efficiency and gain characteristics of strained-layer InGaAs–GaAs quantum-well lasers. *IEEE J. Quant. Electron.* **44**, 732–739 (2008).
55. Haglund, E. et al. 25 Gbit/s transmission over 500m multimode fibre using 850nm VCSEL with integrated mode filter. *Electron. Lett.* **48**, 517–519 (2012).
56. Henry, C. H. Theory of the linewidth of semiconductor lasers. *IEEE J. Quant. Electron.* **18**, 259–264 (1982).
57. Zhao, Y. et al. Spontaneous emission factor for semiconductor superluminescent diodes. *J. Appl. Phys.* **85**, 3945–3948 (1999).

58. Hsieh, P.-Y. et al. Advanced current–voltage model of electrical contacts to GaAs-and Ge-based active silicon photonic devices. *IEEE Trans. Electron Devices* **70**, 4274–4279 (2023).
59. Caer, C. GaAs nano-ridge laser diodes fully fabricated in a 300 mm CMOS pilot line. *Zenodo* https://doi.org/10.5281/zenodo.13286360 (2024).
60. Lv, Z. et al. Ultra-high thermal stability InAs/GaAs quantum dot lasers grown on on-axis Si (001) with a record-high continuous-wave operating temperature of 150 °C. *Opt. Express* **31**, 24173–24182 (2023).

Competing interests The authors declare no competing interests.

Additional information
Supplementary information The online version contains supplementary material available at https://doi.org/10.1038/s41586-024-08364-2.
Correspondence and requests for materials should be addressed to Charles Caer, Didit Yudistira, Bernardette Kunert or Joris Van Campenhout.
Peer review information *Nature* thanks Kirsten Moselund, Ting Wang and the other, anonymous, reviewer(s) for their contribution to the peer review of this work.
**Reprints and permissions information** is available at http://www.nature.com/reprints.
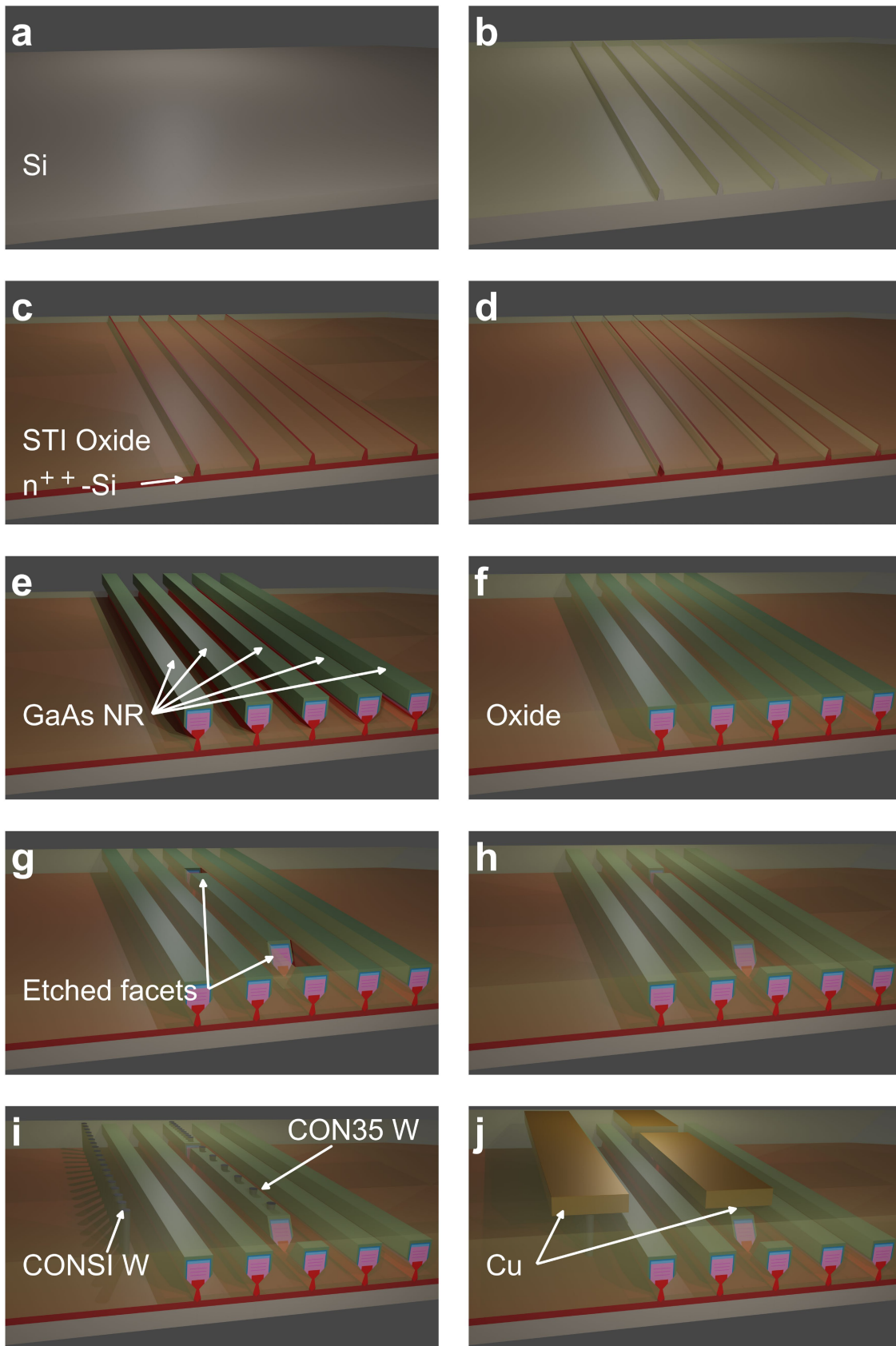
Extended Data Fig. 1 | Summarized process flow of the nano-ridge device fabrication. a, Starting with a 300 mm silicon wafer (001). **b**, Silicon ridge patterning. **c**, STI oxide deposition and n^{++}-implantation. **d**, Si trench patterning. **e**, MOVPE growth of nano-ridges. **f**, Oxide deposition and planarization. **g**, III-V dry etch, oxide deposition and planarization. **h**, Oxide redeposition and planarization. **i**, W plug contact formation. **j**, Cu damascene metallization.
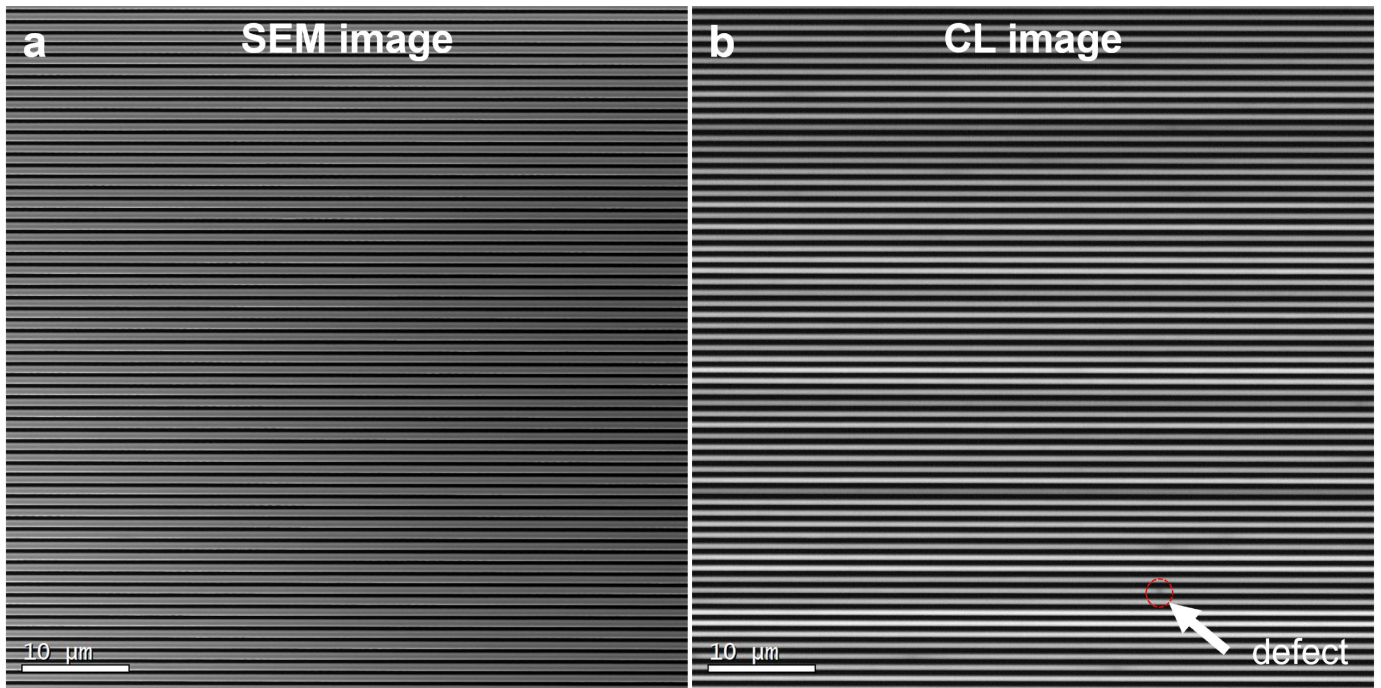
Extended Data Fig. 2 | Nano-ridge defect density imaging. a, Scanning electron microscope (SEM) image of the surface of an array of NRs. **b**, Cathodoluminescence (CL) image of the same area, showing only a single defect in an area covering more than 60×60 μm^2, assessing the very low threading dislocation density in our NR devices.
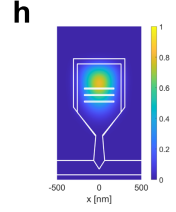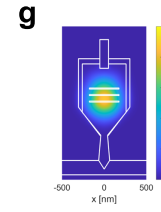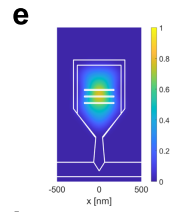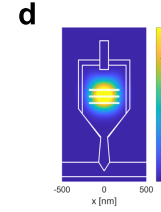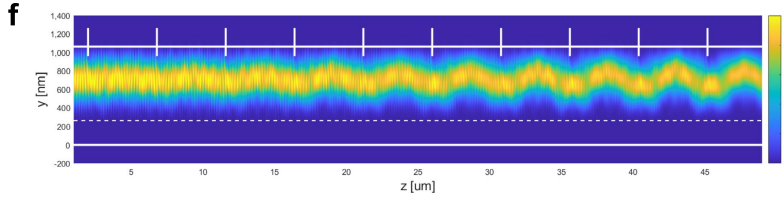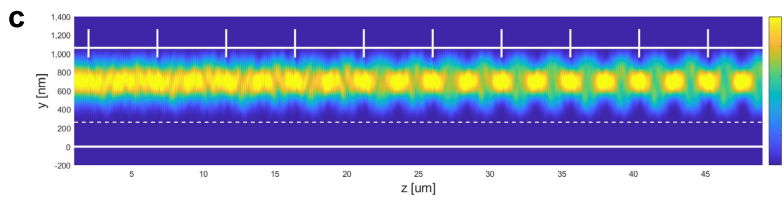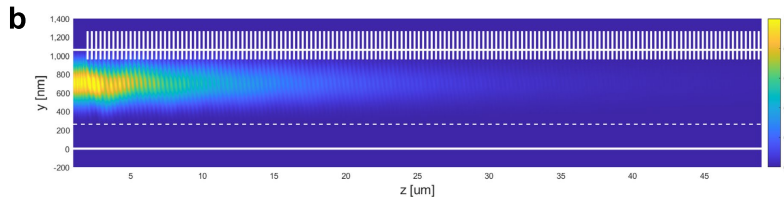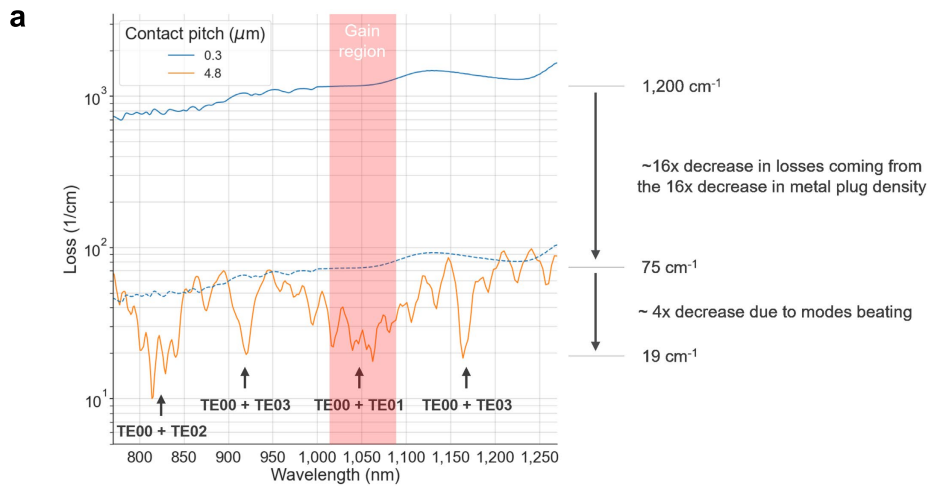
Extended Data Fig. 3 | Mode beating engineering to reduce optical loss in the nano-ridge. a, W contact induced loss as function of wavelength in the case of a dense pitch of 0.3 μm (blue) and in the case a sparse pitch of 4.8 μm (orange) for the plug array, showing nearly two orders of magnitude reduction in the absorption loss near 1,050 nm. The dashed blue line is obtained by dividing the dense pitch losses by 16, in agreement with the baseline from the sparse contact pitch loss spectrum, while the red shaded region shows the extension of the material gain. **b**, Simulated electric field propagation along the z axis for a contact period of 300 nm. **c**, Mode profile for the beating of the TE_{00} and TE_{01} modes at a wavelength of 1,045 nm. **d-e**, Corresponding cross-sections underneath and in between the contact plugs. **g**, Beating mode profile for the TE_{00} and TE_{02} modes at a wavelength of 815 nm. **g-h**, Corresponding cross-sections underneath and in between the contact plug.
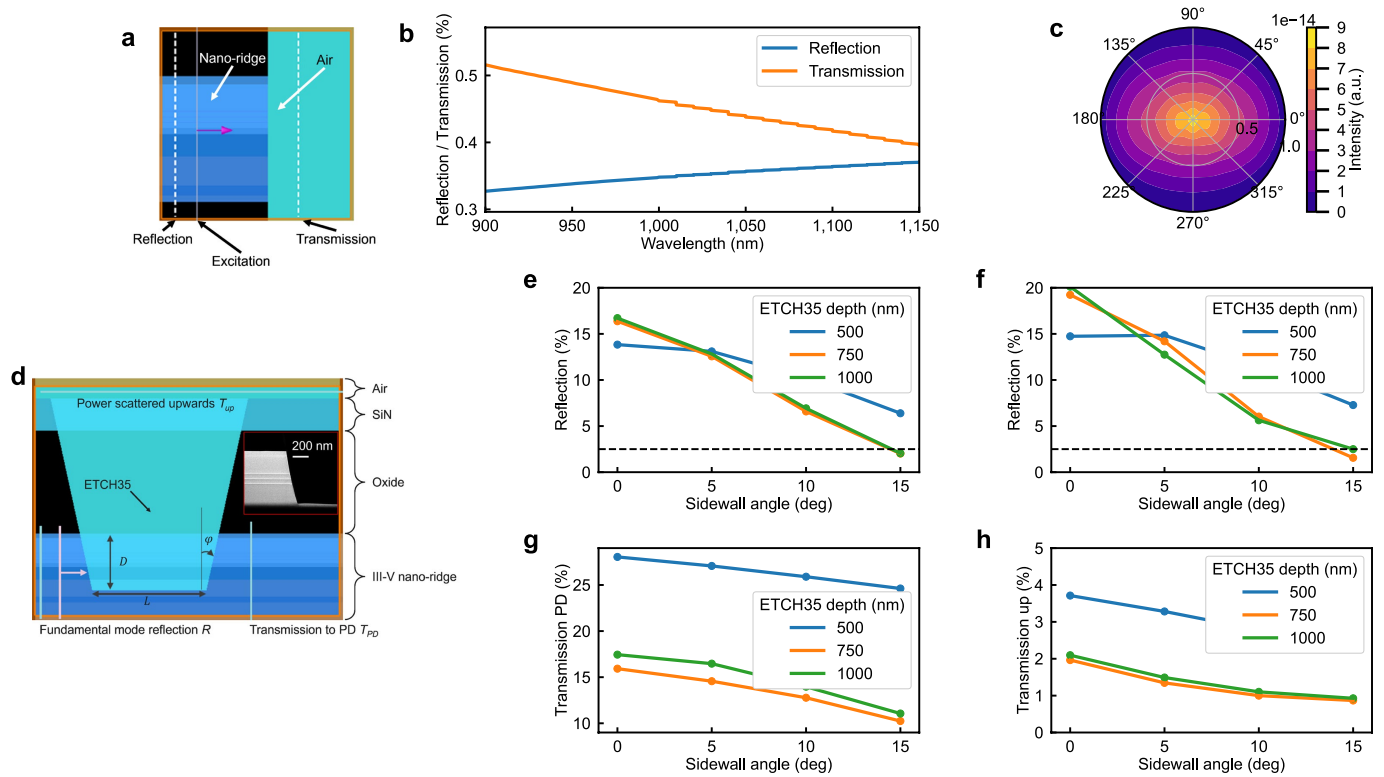
Extended Data Fig. 4 | Nano-ridge facet outcoupling. a, Cross-section of the simulated cleaved facet along the propagation axis, with the broad Gaussian source directly launched in the NR and the two monitors to detect the transmitted and reflected part of the beam. **b**, Reflection and transmission spectrum after incidence on a cleaved facet. **c**, Simulated far-field profile of the beam radiated by the NR cleaved facet. **d**, Cross-section of the simulated structure along the propagation axis, with the broad Gaussian source directly launched in the NR and the three monitors to detect the transmitted and reflected part of the beam along the NR axis, as well as the power scattered upwards, emulating the case of light collection with a multi-mode fibre. Inset shows an HAADF-STEM picture of an etched facet, showing an etch depth around 1,000 nm and a sidewall angle of 12°. **e**, Facet reflection as a function of sidewall angle for various etch depths D in the case of a gap $L = 4 \mu m$. **f**, Facet reflection as a function of sidewall angle for various etch depths D in the case of a gap $L = 1 \mu m$. **g**, Transmission into the inline photodiode as a function of sidewall angle for various etch depths. **h**, Power radiated into free space as a function of sidewall angle for various etch depths D in the case of a gap $L = 4 \mu m$.
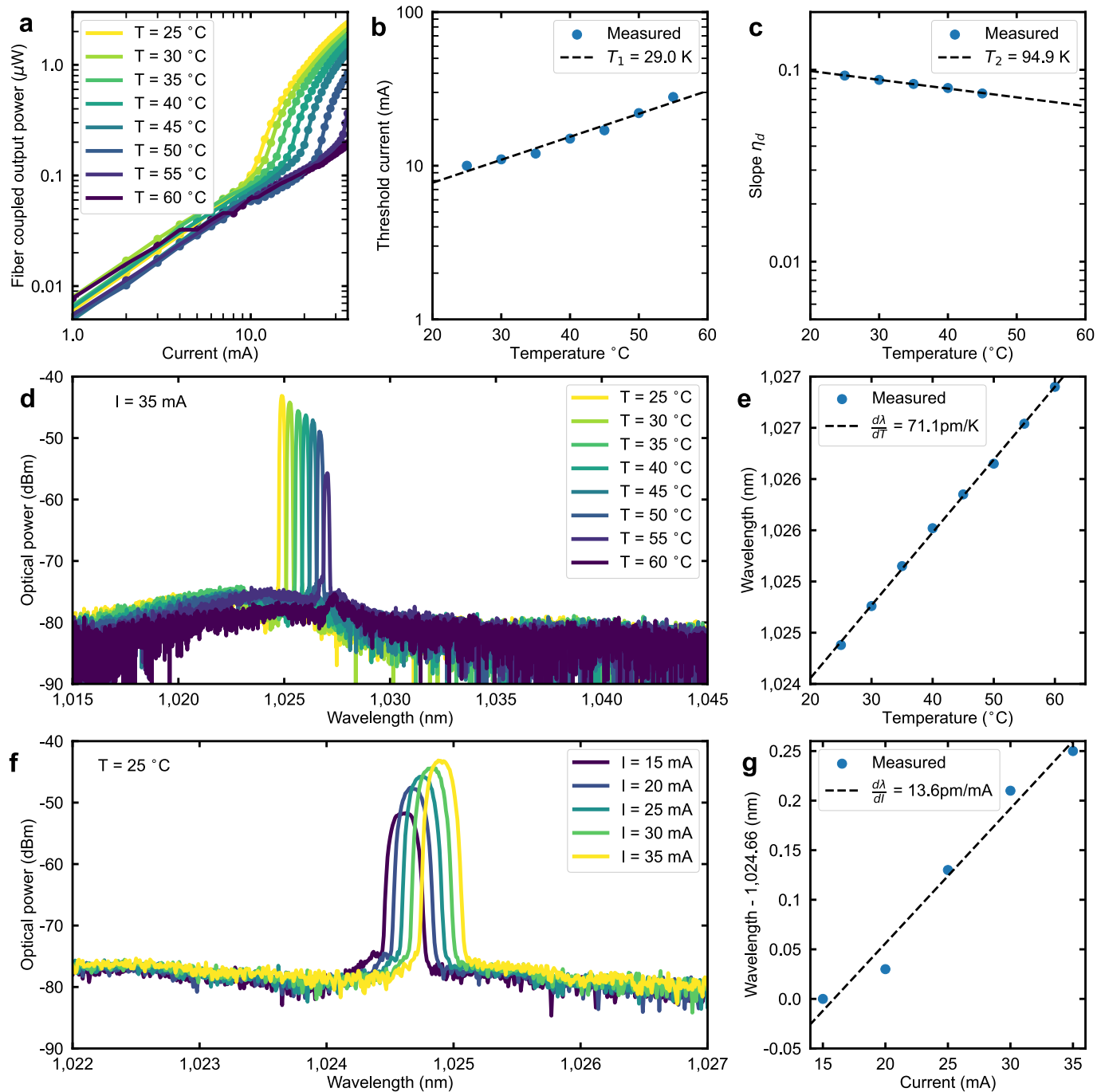
Extended Data Fig. 5 | Temperature and current-dependent measurements of a 2-mm long single-mode NR laser. a, L-I characteristics for temperatures ranging from 25 to 60 °C, showing the large spontaneous emission below threshold. **b,** Threshold current as a function of temperature extracted from **a,** yielding a characteristic temperature T_1 of 29.0 K. **c,** Slope η_d as a function of temperature extracted from **a,** yielding a characteristic temperature T_2 of 94.9 K. **d,** Optical spectra at a current of 35 mA for temperatures ranging from 25 °C to 60 °C, showing SMSR exceeding 20 dB up to 55 °C, while the laser is at threshold when tested at 60 °C. **e,** Laser wavelength as a function of temperature, showing a linear slope of 71.1 pm/K extracted from the optical spectra in **d.** **f,** Optical spectra at a temperature of 25 °C for currents ranging from 20 mA to 35 mA, showing a SMSR exceeding 30 dB. **g,** Laser wavelength as a function of current, showing a linear slope of 13.6 pm/mA extracted from the optical spectra in **f.**
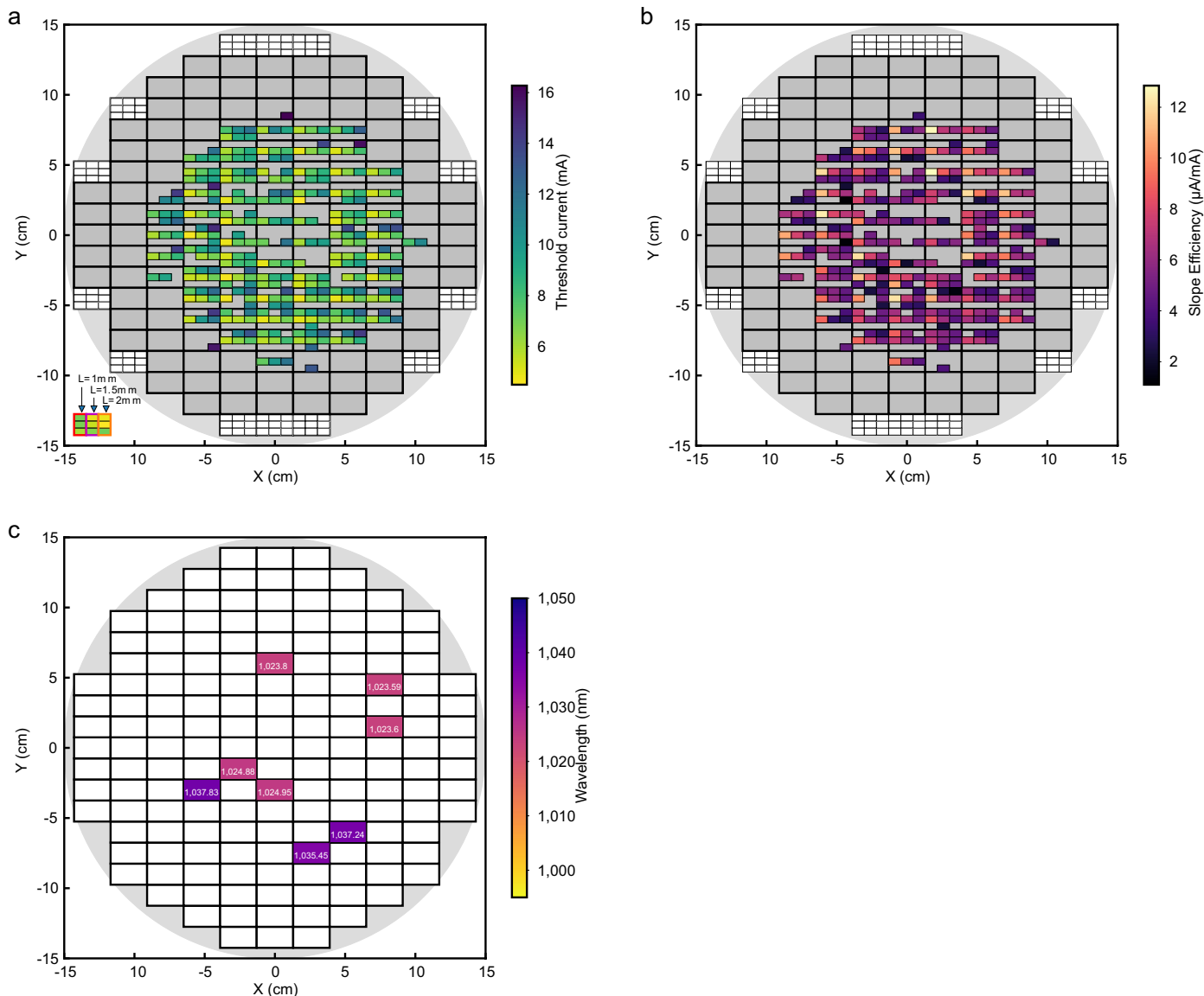
Extended Data Fig. 6 | Wafer maps of the threshold current, mean slope efficiency and wavelength distribution. a, Wafer map of the measured threshold current. Each die is divided in 9 cells grouped in three columns standing for each laser length (1 mm, 1.5 mm and 2 mm), as indicated in the left corner. **b**, Wafer map of the slope efficiency for the same devices. In **a** and **b**, the devices in untested dies and non-working devices are displayed in white and grey, respectively. The tested devices amount to more than 1,200 devices. **c**, Wavelength distribution of 8 identical 2-mm-long lasers across the wafer, showing a wavelength range of less than 15 nm around 1,030 nm from centre to mid-part of the wafer.
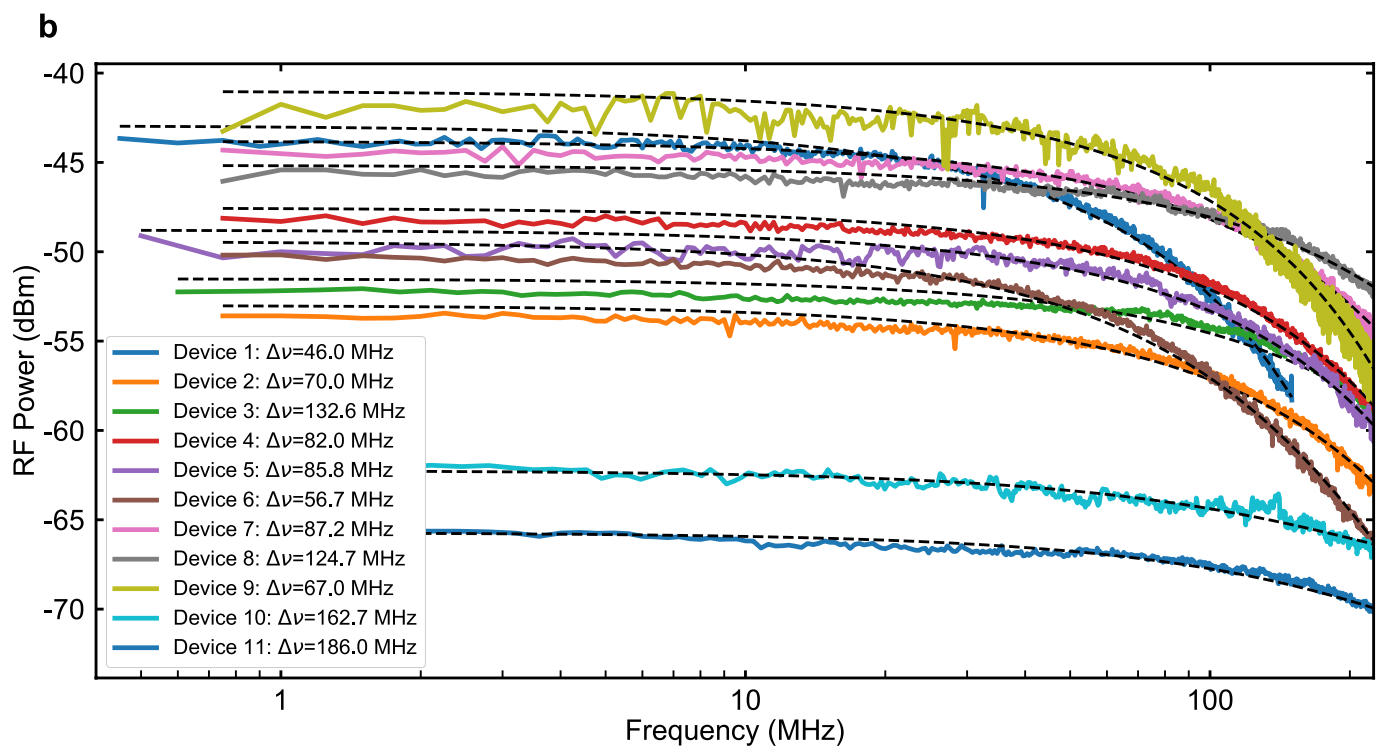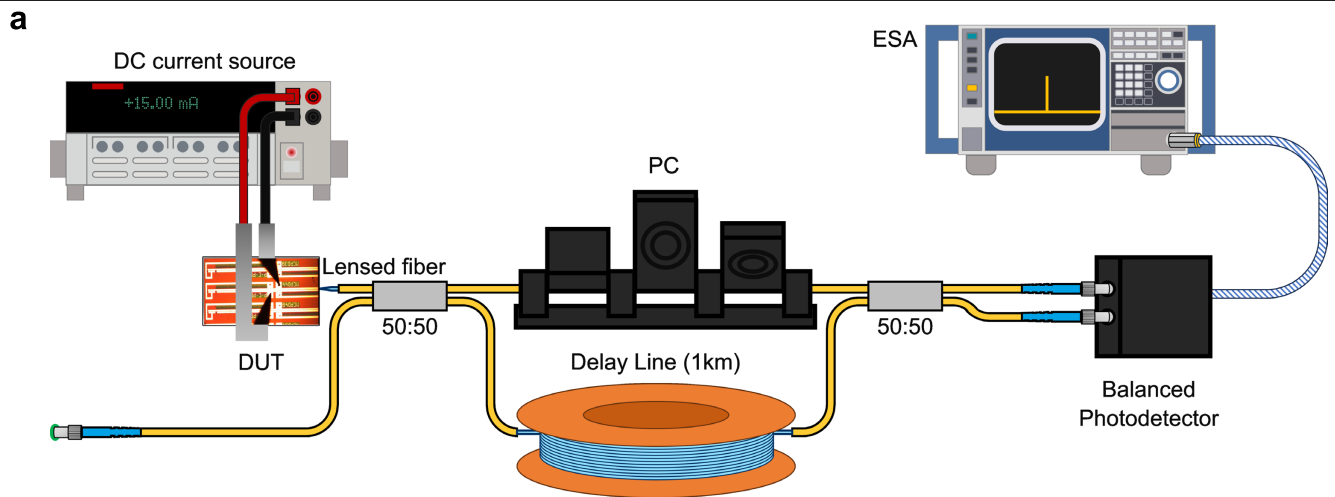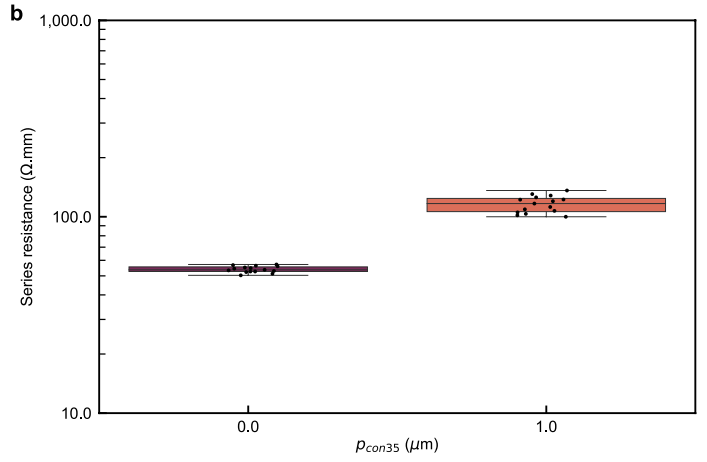
Extended Data Fig. 7 | Laser linewidth measurements by self-homodyne detection. a, Schematic of the self-homodyne interferometric setup used to measure the laser linewidth. **b**, Electrical spectra of 11 measured lasers with superimposed Voigt fit (dashed lines).
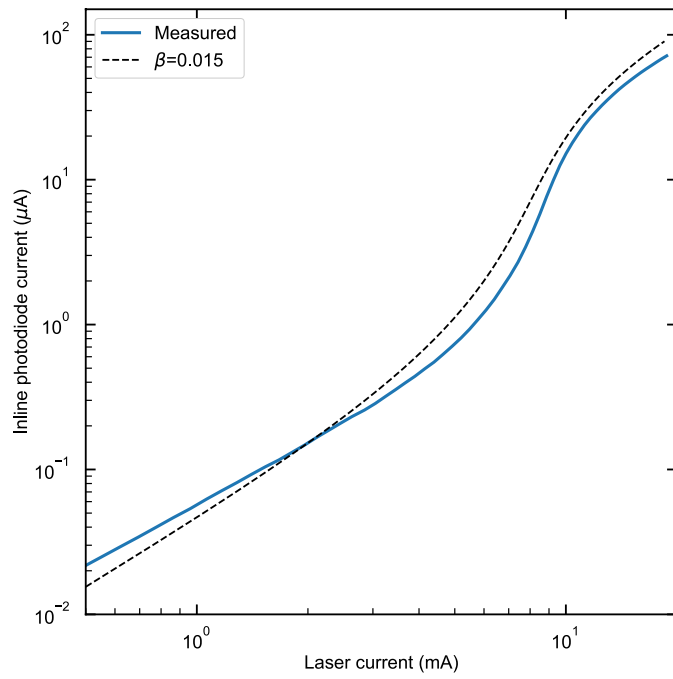
Extended Data Fig. 8 | Nano-ridge spontaneous emission below threshold.
I-I plot of a 2-mm-long laser (blue solid line) extracted from inline photocurrent readout below and above threshold, showing good agreement with a modelled laser with a spontaneous emission factor $\beta = 0.015$ (black dashed line).
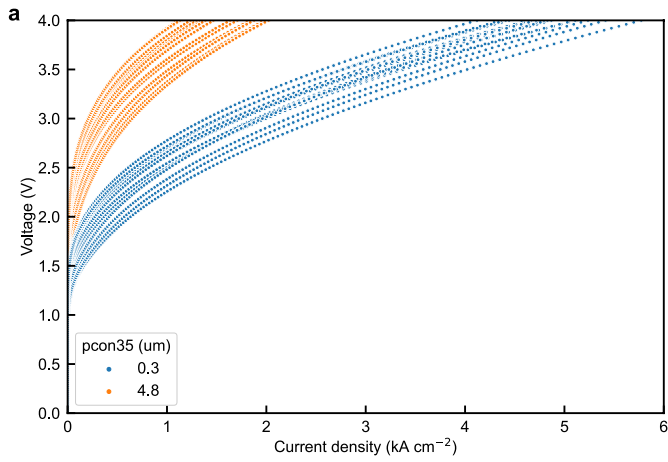
Extended Data Fig. 9 | Extraction of laser series resistance. a, J-V characteristics measured across the wafer for a p-contact W plug pitch (p_{con35}) of 0.3 μm (blue) and 4.8 μm (orange), showing an increase of diode voltage for the case of sparse W plugs, up to 4 V at current density $J = 1$ kA cm^{-2}. **b,** Extracted series resistance, showing a two-fold increase in series resistance when $p_{con35} = 4.8$ μm compared to $p_{con35} = 0.3$ μm.

Article

Extended Data Table 1 | Benchmarking of nano-ridge engineering with other hetero-epitaxy approaches

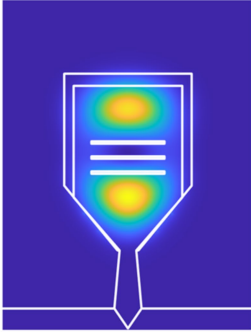| Reference	Wafer size for III-V growth	Growth step	Si substrate	III-V stack thickness	Misfit defect density	Device performance	Output power	Slope efficiency	III-V material	Wavelength
Our present work	300 mm	MOVPE	on pattern – selective	<1 µm	6×10^4 cm^{-2}	cw up to 55 ℃	1.75 mW	Up to 0.5 W/A	$In_{0.2}Ga_{0.8}As$-GaAs QW	1,024 nm
Shang et al. [29]	300 mm	MOVPE + MBE	on pattern – not selective	5.6 µm	1.5×10^7 cm^{-2}	cw up to 60 ℃	127 mW	0.108 W/A	InAs-GaAs QD	1,300 nm
Wei et al. [30]	SOI coupons	MBE (Si) + MBE (III-V)	on pattern – not selective	>7 µm	2.6×10^7 cm^{-2}	cw up to 95 ℃	37 mW	0.148 W/A	InAs-GaAs QD	1,300 nm
Lv et al. [60]	Si/GaP coupons	MBE	blanket	>5.5 µm	4.3×10^6 cm^{-2}	cw up to 150 ℃	100 mW	0.2 W/A	InAs-GaAs QD	1,315 nm
Shang et al. [28]	Si/GaP coupons	MBE	blanket	3.6 µm	1.5×10^6 cm^{-2}	cw up to 108 ℃	65 mW	0.158 W/A	InAs-GaAs QD	1,300 nm

Data from refs. 28–30,60.

Extended Data Table 2 | Summary of the nano-ridge laser performances

Length (mm)	Laser count	Min. I_{th} (mA)	Max. I_{th} (mA)	Mean I_{th} (mA)	Min. slope (µA/mA)	Max. slope (µA/mA)	Mean slope (µA/mA)	Max. out. power (mW)	Max. Wall-Plug Efficiency
1	87	4.49	8.19	5.97	4.23	12.85	8.56	1.32 (at I_{bias}=9.3 mA)	3.3%
1.5	105	5.58	13.6	8.35	2.15	9.61	5.61	1.59 (at I_{bias}=14.4 mA)	2.2%
2	113	6.69	16.27	9.99	1.09	7.06	4.55	1.76 (at I_{bias}=18.76 mA)	2%

Extended Data Table 3 | Simulation of nano-ridge cross-section supporting multiple higher order modes at λ=1,050 nm

TE mode Number	TE$_{00}$	TE$_{01}$	TE$_{10}$	TE$_{02}$	TE$_{03}$
Mode profile at 1,050 nm					
Effective index	3.29	3.08	2.92	2.76	2.31
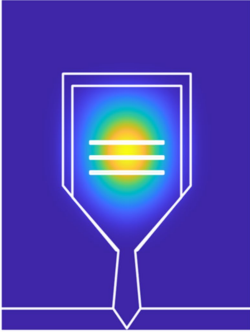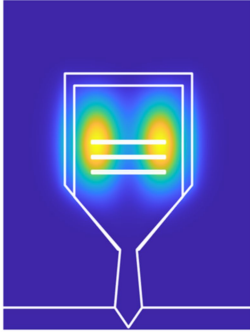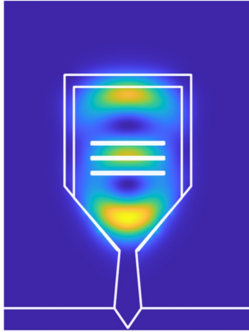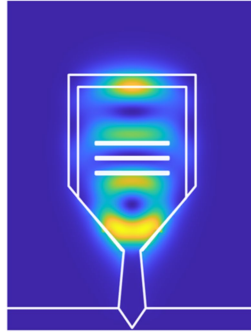
Extended Data Table 4 | Summary of the nano-ridge device parameters for laser rate equations

Parameter	Definition	Value	Source
η_i	QW injection efficiency	0.85	TCAD simulations
q	Electron charge	$1.6021892 \times 10^{-19}$ C	Fundamental constant
V_a	Active volume	$N_{QW} \times h_{QW} \times W_{QW} \times L$	HAADF-STEM
N_{QW}	Number of quantum wells	3	HAADF-STEM
h_{QW}	Quantum well thickness	12 nm	HAADF-STEM
W_{QW}	Quantum well width	400 nm	HAADF-STEM
L	Laser length	1, 1.5 and 2 mm	Designed
A	Shockley-Read-Hall coefficient	4×10^7 s	From measurement fit
B	Bimolecular recombination coefficient	1×10^{-10} cm^3 s^{-1}	Ref. 53
C	Auger recombination coefficient	3.5×10^{-30} cm^6 s^{-1}	Ref. 53
v_g	Group velocity	$\frac{c}{n_g} \sim 0.25c$	Ansys Lumerical Simulations
g_0	Gain coefficient	1,200 cm^{-1}	Ref. 54
N_{tr}	Transparency carrier density	1.8×10^{18} cm^{-3} s^{-1}	Ref. 54
Γ	Confinement factor	$N_{QW} \times \Gamma_0 = 0.08$	Ansys Lumerical Simulations
R_1	Etched facet reflection coefficient	0.05	Ansys Lumerical Simulations
R_2	Etched / cleaved facet reflection coefficient	0.05 / 0.35	Ansys Lumerical Simulations
α_m	Mirror loss	$\frac{1}{L} \log\left(\frac{1}{\sqrt{R_1 R_2}}\right)$	Ansys Lumerical Simulations
α_i	Internal loss	57 cm^{-1}	Ansys Lumerical Simulations
γ_p	Photon decay rate	$v_g \times (\alpha_m + \alpha_i) = 0.5432$ THz	Ansys Lumerical Simulations
β	Spontaneous emission factor	1.5×10^{-2}	From measurement fit (see Ext. Data Fig. 8)

Data from refs. 53,54.

nature research

Corresponding author(s): Charles Caer

Lasing Reporting Summary

Nature Research wishes to improve the reproducibility of the work that we publish. This form is intended for publication with all accepted papers reporting claims of lasing and provides structure for consistency and transparency in reporting. Some list items might not apply to an individual manuscript, but all fields must be completed for clarity.

For further information on Nature Research policies, including our data availability policy, see Authors & Referees.

▶ Experimental design

Please check: are the following details reported in the manuscript?

1. Threshold

   Plots of device output power versus pump power over a wide range of values indicating a clear threshold

   ☒ Yes ☐ No

   In Fig. 3a, Fig. 4a,b and Fig. 5a-c, as well as Extended Data Fig. 5a and 8. Also mentioned in the main text

2. Linewidth narrowing

   Plots of spectral power density for the emission at pump powers below, around, and above the lasing threshold, indicating a clear linewidth narrowing at threshold

   ☒ Yes ☐ No

   We report plot of the spectral power density below, around and above threshold in Fig. 3b.

   Resolution of the spectrometer used to make spectral measurements

   ☐ Yes ☒ No

   Linewidth above threshold is measured with a self-homodyne setup (see Fig. 4c in the main text), alleviating any doubt about the nature of our lasers. The setup is described in Methods and depicted in Extended Data Fig. 7a.

3. Coherent emission

   Measurements of the coherence and/or polarization of the emission

   ☒ Yes ☐ No

   Linewidth above threshold is measured with a self-homodyne setup (see Fig. 4c in the main text). We report a linewidth of 46 MHz. TThe setup is described in Methods and depicted in Extended Data Fig. 7a.

4. Beam spatial profile

   Image and/or measurement of the spatial shape and profile of the emission, showing a well-defined beam above threshold

   ☐ Yes ☒ No

   Due to the small cross-section of the laser, the beam divergence makes it too difficult to image the far field beam profile with an infrared camera. Moreover, our linewidth measurements is a sufficient proof about the lasing properties of our devices.

5. Operating conditions

   Description of the laser and pumping conditions
   Continuous-wave, pulsed, temperature of operation

   ☒ Yes ☐ No

   We describe the measurement conditions in the main text and methods sections. The lasers are probed with DC current with different temperatures (from 25 °C up to 60 °C) and emit in continuous-wave.

   Threshold values provided as density values (e.g. W cm^{-2} or J cm^{-2}) taking into account the area of the device

   ☒ Yes ☐ No

   We report in the main text threshold current densities around 1kA/cm2

6. Alternative explanations

   Reasoning as to why alternative explanations have been ruled out as responsible for the emission characteristics
   e.g. amplified spontaneous, directional scattering; modification of fluorescence spectrum by the cavity

   ☐ Yes ☒ No

   We have performed a self-homodyne measurement with a fibered Mach-Zehnder Interferometer containing a delay line of 1 km in one arm to directly measure the laser linewidth, enabling us to rule out any other explanation.

7. Theoretical analysis

   Theoretical analysis that ensures that the experimental values measured are realistic and reasonable
   e.g. laser threshold, linewidth, cavity gain-loss, efficiency

   ☒ Yes ☐ No

   We have overlayed computed L-I curves from laser rate equation model to the measured data, and found good agreement between the two. Our theoretical analysis is described in the Methods section.

8. Statistics

   Number of devices fabricated and tested

   ☒ Yes ☐ No

   We have fabricated more than 10,000 devices on a 300 mm wafer, including test structures and monitor photodiodes. We have tested 1340 devices, from which we could infer more than 300 working lasers. L-I plots of all working lasers are reported in Fig. 5a-c with a laser count for three different laser length (1 mm, 1.5 mm and 2 mm).

Statistical analysis of the device performance and lifetime (time to failure)

☒ Yes
☐ No

We report an early reliability assessment in the main text, with a lifetime exceeding 500 h of cw operation, as shown in Fig. 4c. We also report in Fig. 5d,e statistics on the threshold current and slope efficiency of all the working lasers in Fig. 5a-c.